Nature Communications

https://doi.org/10.1038/s41467-026-70508-x

Article in Press

In situ synchrotron X-ray scattering reveals organic-mediated scaling mechanisms on desalination membranes

Received: 31 May 2025

Accepted: 26 February 2026

Cite this article as: Feng, Z., Xu, S., Cao, J. *et al.* In situ synchrotron X-ray scattering reveals organic-mediated scaling mechanisms on desalination membranes. *Nat Commun* (2026). https://doi.org/10.1038/s41467-026-70508-x

Zimou Feng, Shu Xu, Jingjing Cao, Zhen Ren, Yi Yang, Jin Jiang, Xunda Feng & Xinglin Lu

In Situ Synchrotron X-ray Scattering Reveals Organic-Mediated Scaling Mechanisms on Desalination Membranes

Zimou Feng[1,†], Shu Xu[1,2,†], Jingjing Cao[1,3], Zhen Ren[1], Yi Yang[1], Jin Jiang[4], Xunda Feng[5], and Xinglin Lu[*,1,6]

1. State Key Laboratory of Advanced Environmental Technology, Department of Environmental Science and Engineering, University of Science and Technology of China, Hefei 230026, China.

2. SCNU Environmental Research Institute, Guangdong Provincial Key Laboratory of Chemical Pollution and Environmental Safety & MOE Key Laboratory of Theoretical Chemistry of Environment, School of Environment, South China Normal University, Guangzhou 510006, China.

3. College of Textile Science and Engineering, Jiangnan University, Wuxi 214122, China.

4. Guangdong Basic Research Center of Excellence for Ecological Security and Green Development, Key Laboratory for City Environmental Safety and Green Development of the Ministry of Education, School of Ecology, Environment and Resources, Guangdong University of Technology, Guangzhou 510006, China

5. State Key Laboratory of Advanced Fiber Materials, Center for Advanced Low-dimension Materials, and College of Materials Sciences and Engineering, Donghua University, Shanghai 201620, China.

6. National Synchrotron Radiation Laboratory, University of Science and Technology of China, Hefei 230026, China.

† These authors contributed equally.

* Corresponding Author
E-mail: xinglinlu@ustc.edu.cn

Abstract.

Inorganic scaling, governed by complex organic–inorganic interactions, presents a pervasive challenge in aqueous environments with broad implications for engineering systems. Using reverse-osmosis (RO) desalination as a model platform, we investigate how mixed organic foulants influence inorganic gypsum scaling at membrane–water interfaces. Representative proteins, humic substances, and polysaccharides are employed as model foulants to reveal their roles in modulating gypsum crystallization behavior. By integrating advanced *in situ*, time-resolved synchrotron X-ray scattering within the concentration polarization layer—a region typically inaccessible to conventional characterization techniques—with modelling, spectroscopic, and imaging analyses, we track the evolution of gypsum scaling from nanoscale precursors to mature crystals. Our findings reveal that different classes of organic foulants regulate gypsum crystallization through distinct mechanisms, ranging from inhibiting precursor aggregation in the bulk solution to altering interfacial physicochemical properties that govern the kinetics of heterogeneous nucleation and growth. These findings provide molecular-level insights into the coupled dynamics of organic fouling and inorganic scaling, advancing mechanistic understanding of crystallization at functional interfaces. Such insights offer guidance for the rational design of anti-scaling strategies in engineering systems.

Introduction

Inorganic scaling, i.e., the crystallization of sparingly soluble salts, is a widespread phenomenon observed across both natural and engineered systems[1]. During crystallization, a disordered phase in a supersaturated solution transforms into a highly ordered, periodic lattice. This process proceeds through two fundamental stages: nucleation and subsequent crystal growth. Nucleation constitutes the critical, rate-determining step of this first-order phase transition, wherein the smallest thermodynamically stable nuclei of the new crystalline phase emerge. In the natural systems, scaling regulates long-term carbon and sulfur cycles through geochemical processes such as marine carbonate precipitation[2] and the formation of travertine terraces at geothermal springs[3], thereby shaping mineral landscape of the Earth. In the engineered systems, such as membrane-based desalination[4-6], electrochemical reactors[7], and energy storage devices[8,9], scaling poses significant challenges to operating efficiency as the presence of scaling layers substantially inhibit mass or heat transfers[10,11]. Even a minimal scale accumulation—on the order of few millimeters—can elevate energy demands for operation, leading to considerable economic and environmental costs[12,13]. For instance, in reverse osmosis (RO) seawater desalination processes, managing inorganic scaling through antiscalant dosing, periodic cleaning, and module replacements can account for over 25% of operating costs[12]. Such fact thus necessitates effective scaling control strategies for the engineering systems.

Precise design of scaling control strategies relies on the mechanistic insights into interfacial scaling pathways[13]. Despite the pervasive occurrence of scaling, the fundamental physicochemical mechanisms governing scale nucleation, phase selection, and crystal growth at solid-liquid interfaces remain inadequately understood—particularly realistic water chemistries containing complex organic substances[16,17]. As a consequence, conventional scaling control strategies in engineering systems are largely based on trial-and-error approaches[14-17], highlighting the urgent need for mechanistic understanding to enable rational design of effective anti-scaling strategies.

Scaling typically proceeds via two distinct mechanisms: homogeneous nucleation and crystal growth in bulk solution, and heterogeneous nucleation and crystal adhesion to surfaces[17,22]. These pathways are dynamically coupled at the nano- to microscale regimes for the formed nucleates and crystals. Both experimental and theoretical studies suggest that crystallization can proceed through

different dominant nucleation pathways, including classical descriptions based on direct ion-by-ion assembly into a crystalline nucleus[18] and non-classical, precursor-mediated scenarios, characterized by the formation of pre-nucleation clusters[19], amorphous precursor assembly[20], and subsequent structural rearrangement[21]. Distinguishing the dominant nucleation pathway under specific conditions is critical for revealing scaling behaviors and developing control strategies. For example, in systems where ion-by-ion attachment plays a primary role, inhibitors function primarily by reducing supersaturation or chelating free ions to suppress nucleation[22], while in systems governed by precursor-mediated nucleation, inhibitors could elevate interfacial energy barriers to prevent lattice matching and subsequent crystal growth on surfaces[23]. The challenge is further compounded by the complex water matrices, which do not contain inorganic salts alone[24]. The inevitable presence of natural organic matter[25], extracellular polymers[26], and biomineralization agents[27] creates mixed fouling environments, where organic–inorganic interactions modulate interfacial energy barriers, shield nucleation sites, or promote alternative crystallization pathways[28]. These interactions can lead to distinct morphologies and deposition dynamics compared to pure inorganic scaling. Therefore, developing cross-scale, *in situ* characterization methods[29], together with advancing in multiphysics simulations[30], is essential to delineate the dominant scaling pathways, as well as their synergistic or antagonistic effects under mixed fouling conditions.

Traditional analytical methods for studying scaling—such as flux decay measurements, *ex situ* imaging or spectroscopic techniques—are inherently limited in their ability in capturing dynamic processes. These approaches typically provide only static snapshots or time-averaged data. Such limited spatiotemporal resolution prevents *in situ* characterization of nucleation pathways and aggregation dynamics during the early stages of scaling. Moreover, most of these approaches involve destructive procedures in sample preparation, such as vacuum drying or metal coating, which likely disrupt the native structure of scaling layers and complicate the direct observation of interactions among organic foulants and inorganic phases.

In contrast, synchrotron radiation-based techniques offer distinct advantages for investigating scaling dynamics in complex aqueous systems[31,32]. Specifically, small-angle and wide-angle X-ray scattering (SAXS/WAXS) utilize high brightness and precise monochromaticity to enable *real-time* observations of homogeneous crystallization processes in supersaturated solutions[33,34]. By

simultaneously acquiring SAXS and WAXS data from the same sample, these scattering techniques provide reciprocal-space coverage from nanometer to sub-micrometer scales[35,36], allowing for quantitative analysis of structural transitions—from amorphous pre-nucleation states detected by SAXS to crystalline phases characterized by distinct Bragg peaks in WASX[37,38]. This approach yields continuous, multiscale analysis of complex fouling processes, bridging molecular to mesoscopic scales and offering insights into interfacial crystallization dynamics under realistic conditions. Besides these scattering techniques, synchrotron radiation could also be coupled with Fourier-transform infrared (FTIR) mapping to resolve spatial distribution of foulant molecules (i.e., characteristic functional groups) on material surfaces with micrometer-scale resolution[39-42]. The combination of these synchrotron radiation-based techniques (SAXS, WAXS, and FITR mapping) can provide a comprehensive, chemically specific view of scaling formation and transformation at material interfaces, enabling a closer look of both structural and compositional dynamics during the scaling processes.

In this study, we integrated advanced synchrotron radiation techniques with interfacial energy analysis to unravel the complex dynamics of hybrid organic–inorganic scaling. Using gypsum as a model inorganic scalant and three representative organic foulants—bovine serum albumin (BSA), humic acid (HA), and sodium alginate (SA)—we explored both homogeneous crystallization within the concentration polarization (CP) layer and heterogeneous nucleation on the membrane surface. Our characterization approach combines time-resolved small- and wide-angle X-ray scattering to capture, in real time, the transformation from precursor species to crystalline phases. In addition to X-ray scattering, our approach was further complemented by quartz crystal microbalance with dissipation monitoring (QCM-D) and extended DLVO (XDLVO) theory to quantify interfacial interactions. By synchronizing multiscale structural characterization with interfacial energy landscape analysis, we identified how organic–inorganic interactions regulate scaling behavior—ranging from delayed nucleation to altered crystal growth directions and morphologies. Notably, we revealed that gypsum crystallization under RO conditions proceed via a non-classical precursor-mediated nucleation pathway, characterized by metastable precursor clusters prior to the emergence of long-range crystalline order. This observation contrasts with the direct ion-by-ion assembly typically described within classical nucleation frameworks. We further demonstrate that organic co-foulants modulate the early-stage nucleation behavior by acting as

molecular "switches" that redirect the dominant crystallization pathway under RO conditions. Our findings offer a mechanistic foundation for predicting and controlling mixed fouling in membrane systems, representing a significant step toward the rational design of antifouling strategies in water treatment, energy conversion, and other interface-dependent technologies.

Results

Impact of organic foulants on gypsum scaling.

To investigate the influence of organic foulants on gypsum scaling, we conducted membrane scaling experiments using a lab-scale reverse osmosis (RO) system. The feed solutions consisted of 30 mM calcium chloride ($CaCl_2$) and 30 mM sodium sulfate (Na_2SO_4), resulting in a supersaturation ratio (SR) of 1.71, corresponding to a **supersaturation index (SI)** of 0.234. Under these bulk conditions, the theoretical induction time for gypsum scaling, when estimated using an idealized classical nucleation model neglecting wall effects and impurities, suggests a relatively long duration. Despite the potential for bulk nucleation under specific conditions[43-45], no visible crystals or turbidity were observed in the feed tank during the 24-hour experiment. This observation confirms that spontaneous crystallization did not occur in the bulk phase under the experimental conditions employed in this study. However, due to the presence of concentration polarization at the membrane surface, the gypsum SR rose to 10.05 (SI =1.002) (Supplementary Note 2), significantly reducing the induction time to ~4 minutes[46,47]. This finding indicates that gypsum scaling occurs exclusively within the concentration polarization layer, rather than from spontaneous crystallization in the bulk solution. For comparison, we also examined flux decline in the presence of organic foulant alone, allowing for a direct evaluation of individual foulants to membrane fouling.

Figure 1 illustrates the membrane flux decline caused by gypsum scaling alone and gypsum-organic mixed fouling in the presence of different organic foulants. Pure gypsum fouling (grey triangles) led to complete flux loss within 4.04 ± 0.06 hours. In contrast, mixed fouling with gypsum and bovine serum albumin (BSA, dark blue squares in Figure 1a) exhibited a significantly slower flux decline, with a reduction of 46.18% ± 0.54% after 6 hours, indicating that BSA effectively inhibits gypsum scaling. Mixed fouling with gypsum and humic acid (HA, dark orange

squares in Figure 1b) caused a flux decline of 92.27% ± 0.25% after 6 hours, suggesting that HA moderates the severity of flux loss compared to pure gypsum scaling. For sodium alginate (SA) and gypsum mixed fouling (dark red squares in Figure 1c), the initial flux decline mirrored the trend observed for pure gypsum; however, the rate slowed as flux decreased, ultimately leading to in complete flux loss after 9.00 ± 0.12 hours. These findings indicate that SA also mitigates gypsum scaling during operation. Overall, the flux declines in the mixed fouling systems were less severe than the cumulative effect of pure gypsum (grey triangles) and individual organic foulants (light circles), demonstrating that organic foulants reduce gypsum scaling and alleviate the severity of mixed fouling.

FIGURE 1.

Corresponding SEM images of the fouled membranes (Figure 1d and Supplementary Figure 1) revealed distinct gypsum crystal morphologies influenced by the type of organic foulants. Pure gypsum fouling produced elongated, needle-shaped crystals that were loosely deposited on the membrane surface. In the BSA mixed fouling system, the crystals appeared as short, thick blocks with smooth sides and stepped tops, with minor amounts of protein observed on the crystal surfaces. In the HA mixed fouling system, the crystals formed rosette-like structures with incomplete growth on individual petals and exhibited stepped growth on the side surfaces, resulting in a stacked-flake structure. Additionally, some HA clusters were observed between the crystals. In the SA group, the crystals were encased in alginate gel, forming rosette shapes with longer, thicker prisms, alongside small needle-like and shield-shaped twinned crystals. These observations suggest that while gypsum crystallization remains the primary mechanism of membrane blockage, the presence of organic foulants significantly alters the morphology of gypsum crystals, thereby affecting their nucleation, formation, and growth.

Notably, higher-magnification SEM images (Figure 1e) revealed distinct growth behaviors of gypsum crystals under different conditions. In the case of pure gypsum, the crystals formed well-defined, needle-like crystals with the largest surface area on the (020) side face, while the top face (011) and the other side face (120) were relatively smaller due to the crystal's elongated shape. With the presence of BSA, the crystals became shorter and thicker, exhibiting more balanced proportions of side faces (020) and (120), with steps emerging along the (–102) plane on the top face. In the HA group, the crystals showed incomplete growth on the side faces, alternating (120)

and (111) planes, which significantly reduced the area of the (020) face. In the SA group, shield-shaped twinned crystals, commonly referred to as "Montmartre twins," were observed, with twinning planes aligned along the (–101) plane [48,49].

In situ monitoring of inorganic foulant crystallization processes within the concentration polarization layer.

Rejection of ions in membrane desalination results in the formation of concentration polarization (CP) (Figure 2a). Under the operating conditions used in this study, CP caused calcium sulfate to accumulate on the membrane surface at concentrations 3.9 times higher than those in the bulk solution, corresponding to a gypsum SR of 10.05 (SI =1.002) (Figure 2b). Detailed calculation parameters, including diffusion coefficients and calculated surface concentrations, are provided in Supplementary Table 1. According to the empirical relationship between induction time and supersaturation, such elevated supersaturation levels promotes homogeneous nucleation, initiating gypsum crystallization[47,50,51]. The process of inorganic scaling is time-dependent and involves a series of complex, overlapping microscopic events that occur after the onset of supersaturation, including nucleation, crystal growth, and aggregation. The induction time is defined as the macroscopic time interval between the achievement of supersaturation and the first detectable appearance of the solid phase, thus encompassing these initial, often inseparable, microscopic processes[52,53]. Consequently, real-time monitoring of the CP layer is crucial to understanding the progression of inorganic scaling, especially under the mixed fouling conditions. While conventional techniques such as conductivity and turbidity measurements demonstrate that organic foulants delayed the onset of gypsum crystallization and reduced crystal volume (Supplementary Note 3, Supplementary Figure 5), the low sensitivity of these methods limited further elucidation of crystallization mechanisms.

To gain a deeper understanding of the nucleation and growth dynamics, we employed a time-resolved, synchrotron-based *in situ* X-ray scattering technique to investigate the transformation of nanoscale precursors into macroscopic gypsum crystals (Figure 2c). Notably, these *in situ* SAXS/WAXS measurements were designed to probe the crystallization kinetics within the fluid phase of the CP layer and were performed in a membrane-free configuration. Solutions were

prepared to replicate the ion concentration in the CP layer adjacent to the membrane surface, and a peristaltic pump circulated the reaction mixture through a quartz capillary rather than a membrane module. The crystallization was initiated by injecting calcium chloride ($CaCl_2$) using a remotely controlled syringe pump (Figure 2c_1), ensuring uniform mixing with sodium sulfate ($NaSO_4$). During the measurement, X-ray was propagated through the sample in the quartz tube, and scattering signals were collected by WAXS and SAXS detectors positioned at designated distances (Figure 2c_2). Time-resolved scattering data were collected at intervals of five seconds, capturing the entire sequence of homogeneous crystallization. SAXS images revealed a gradual expansion of the central scattering patterns, while WAXS images displayed emerging diffraction patterns, reflecting the progression from nucleation to crystal growth (Figure 2c_2). This high spatiotemporal resolution approach enables a closer-look of the crystallization dynamics, enabling the tracking of nanoscale precursor development into gypsum crystals until no further changes were observed in the scattering signals.

FIGURE 2.

Supplementary Figure 8 illustrates the raw 2D isotropic SAXS patterns acquired by the detector, which were subsequently integrated into 1D profiles and processed to present the data as time-resolved *in situ* SAXS patterns. The time-resolved SAXS waterfall plots and heatmaps for the four sample groups are displayed in Supplementary Figure 9 and Figure 3a, respectively. The concentration of 85 mM $CaSO_4$ used in Figure 3 represents a characteristic mid-region concentration within the CP layer, lying between the bulk concentration (~30 mM) and the membrane-surface concentration shown in Fig 2b. Data collection began with the injection of calcium chloride and continued until the scattering intensity stabilized over 40 minutes. The stages of scatterer evolution are delineated by dashed lines.

As shown in Figure 3a, throughout the entire crystallization induction period, the scattering intensity in the presence of organic foulants remained consistently lower than that of the pure $CaSO_4$ group. This finding indicates that the organic foulants reduced the effective supersaturation, thereby decreasing both the nucleation density and the number of primary clusters. For the three organic foulants, the signal changes exhibited four distinct SAXS phases, reflecting the continuous evolution of nanoscale scatterers prior to and during crystallization: an initial increase in intensity, a slight decrease followed by stabilization, a significant intensity increase, and final stabilization

at a maximum intensity with a slight decline. In the $CaSO_4$-BSA group (Figure 3a$_2$), Phase 1 (below the blue dashed line) showed an intensity increase within the first 160 seconds. In the HA (Figure 3a$_3$) and SA (Figure 3a$_4$) groups, the initial intensity increase lasted for 40 and 95 seconds, respectively (as indicated by the blue dashed line). The durations of Phase 2—defined as the region between the blue and yellow dashed lines—for BSA, HA, and SA were 590, 340, and 90 seconds, respectively. In contrast, no clear distinction between the first two stages was observed in the pure $CaSO_4$ group (Figure 3a$_1$). This group exhibited an extremely short induction period, followed by a rapid intensity increase across all q values from the beginning of the experiment, making it challenging to differentiate the initial stages. The durations of Phase 3, defined as the region between the yellow and red dashed lines, for the pure $CaSO_4$, BSA, HA, and SA groups were 300, 1615, 345, and 800 seconds, respectively.

FIGURE 3.

Nanoscale particles or regions exhibiting electron density with the surrounding solution (*i.e.*, scatterers) were identified through their contribution to SAXS signal intensity. The dynamic evolution of scatterers during the crystallization process can be illustrated by taking pure $CaSO_4$ as an example. As illustrated in Figure 3b, in Phase **1**, the increase in scattering intensity indicates the formation of scatterers with electron densities distinct from the background solution. In Phase **2**, interactions among primary species led to the formation of small clusters and the development of the system's structure factor, resulting in a slight decrease in scattering intensity. Despite these interactions, the local concentration remained relatively low, and the scatterers were still sparsely distributed. In Phase **3**, scattering intensity increased significantly by several orders of magnitude, reflecting a transition from an initially dispersed arrangement to a denser and more compact structure, implying the growth of clusters. Following this stage, the stacking and merging of clusters reduced the overall surface area, leading to a slight decline in scattering intensity, as depicted in Figure 3c. Taken together, these stages represent the dynamic evolution of scatterers, from initial formation and sparse interactions to cluster densification and eventual structural consolidation.

Figure 3d illustrates the evolution of the power-law dependence between scattering intensity (I) and vector (q). In Phase **1**, the scattering intensity shows an overall increase, indicating the formation of initial scatterers. In Phase **2**, the intensity follows the relationship $I(q) \propto q^{-1}$,

suggesting that the primary scatterers formed in the solution were larger than typical ion pairs[54,55]. During this stage, a slight decrease in intensity at $q > 0.78$ nm^{-1} suggests the aggregation of primary scatterers into larger structures[56]. In Phase **3**, $I(q)$ follows a power-law dependence on q, with an exponent ranging from –3 to –4, reflecting the surface fractal dimension (D_s) of the scatterers, where $I(q) \propto q^{(-6+D_s)}$. A D_s value of 2 indicates smooth surfaces, while a value approaching 3 indicates rough, fractal-like surfaces[53,54]. As such, the increase in D_s suggests that the scatterers develop more irregular and complex surfaces, implying ongoing rearrangement and structural evolution within the system. These observations highlight the dynamic transitions in scatterer structure and surface properties throughout the crystallization process.

All organic foulants significantly prolonged the formation and evolution of primary scatterers during the initial SAXS Phases 1 and 2, corresponding to the crystallization induction period observed by WAXS. In Phase **3**, BSA strongly delayed the formation of larger nuclei, thus effectively inhibiting the aggregation and growth of clusters (Figure 3a$_2$). Although HA and SA displayed similar overall trends, their effects differed across specific stages. In the HA group, Phases **1** and **3** were relatively short, with the prolongation primarily occurring in Phase **2** (Figure 3a$_3$). This behavior is likely due to the weaker ionic binding capacities of HA molecules, which prevented significant suppression of supersaturation. However, as well-dispersed, charged small molecules, HA effectively blocked interactions between primary $CaSO_4$ scatterers, maintaining them in a dispersed state. In contrast, SA formed an irregular gel structure that acted as nucleation sites. While SA failed to suppress scatterer formation in Phase **2**, it delayed cluster growth in Phase **3**, effectively extending this phase (Figure 3a$_4$). At the end of the reaction, the gyration radius of nuclei in the pure $CaSO_4$, HA, and SA groups was ~4 nm, whereas in the BSA group, it was about 2 nm (Figure 3e). Such size difference indicates that BSA most significantly inhibited the growth and aggregation of clusters in the CP-layer solution, while HA and SA exert weaker control over bulk cluster growth.

Supplementary Figure 11 illustrates the integration and processing of the WAXS patterns, showing the procedures in transforming the patterns into time-resolved waterfall plots and heatmaps. The 3D waterfall plots for the four groups are presented in Supplementary Figure 12, providing a clear visualization of the temporal evolution of diffraction signals during the scaling process. As shown in Figure 4a, characteristic peaks of gypsum appeared sequentially across all

simulated concentration polarization layer solutions and intensified over time. By correlating the X-ray wavelength (λ), and diffraction angle (2θ), with q using the Bragg's law ($q = 4\pi\lambda/\sin\theta$), the WAXS data largely aligned with the powder XRD spectrum of gypsum (Supplementary Figure 13), verifying the formation the crystalline gypsum in our system.

FIGURE 4.

During the initial formation and aggregation of primary scatterers, pronounced changes were observed in the SAXS signals across all samples, whereas no WAXS diffraction peaks were detected, indicating the formation of non-crystalline nanoscale precursors. This discrepancy indicates that the system initially contained non-crystalline, nanoscale $CaSO_4$ precursors detectable by SAXS but invisible to WAXS. The aggregation and evolution of these amorphous precursors correspond to the WAXS induction period for gypsum crystallization. The induction time varied among the different organic foulants (Figure 4b). In pure gypsum (without organic foulants), it was less than 100 seconds. In comparison, HA and SA extended the induction time to 550 and 400 seconds, respectively, while BSA caused the longest delay, up to 1,000 seconds. Taking the (020) peak area as an indicator of gypsum crystallinity (Figure 4c), the result showed that all three foulants significantly reduced the crystallization rate of gypsum, leading to different degrees of gypsum crystallinity, in the order of: pure gypsum > SA > HA > BSA. To further explore the time evolution of crystal structure, three distinct stages were identified in the WAXS spectrum (Figure 4d). Stage **I** exhibited no detectable diffraction peaks, corresponding to the induction period during which amorphous precursors formed and evolved, as captured by SAXS Phases 1–2. Stage **II** was characterized by a rapid emergence and growth of characteristic gypsum diffraction peaks, coinciding with SAXS Phase 3, indicating the structural transformation of amorphous clusters into crystalline gypsum. Stage **III** represented the crystal growth phase, where the solution's supersaturation decreased, no new nuclei formed, and the signal intensity increased at a slower rate. Towards the end of the process, a slight decline in diffraction intensity was observed across all groups, likely due to the settling of millimeter-sized crystals at the bottom of the beaker. This settling reduced the number of crystals passing through the quartz tube, thereby lowering the detected signal intensity.

A notable observation was made in the SA group: the first crystallization stage was prolonged (Figure 4b), yet its crystallinity was the highest among the mixed fouling groups (Figure

4c). These results suggest that while SA delays nucleation, it does not suppress subsequent crystal growth. Instead, the strong complexation of SA with Ca^{2+} led to the formation of a gel layer, thereby resisting their interaction with SO_4^{2-} ions. This process lowers the local supersaturation and effectively increases crystal solubility. As a result, nucleation occurs more slowly in the SA group compared to pure gypsum, without significantly altering the subsequent crystal growth dynamics. Such delay, combined with a gel-mediated growth environment, enables continued crystal development, ultimately leading to a higher degree of crystallinity during the later stages of crystallization despite the initial delay. In comparison, BSA and HA both led to delays across all crystallization stages and resulted in a reduction in the degree of crystallinity, likely due to their adsorption onto active sites on crystal surfaces. This adsorption interferes with crystal face growth by blocking key sites for ion attachment, altering the surface energy and leading to irregular crystal morphologies. Additionally, the steric hindrance provided by BSA disrupts crystal stacking and restructuring, further limiting crystallinity.

At the end of the reaction, the crystallite size and the (020)/(021) face ratio are shown in Figure 4e. The crystallite size, i.e., the spatial length perpendicular to the (020) plane (Figure 4e$_1$), remained relatively consistent across both the pure gypsum group and the organic fouling mixed groups (Figure 4f), ranging from 73.44 to 76.73 nm. The (020) plane corresponds to the side facet of gypsum crystals, while the (021) plane corresponds to the top facet (Figure 4e$_2$). The ratio of diffraction intensity between these planes serves as an indicator of the growth direction and overall morphology of the gypsum crystals[57]. In the WAXS signals obtained from the four supersaturated solutions, the (020)/(021) facet ratio remained largely unchanged and eventually stabilized at approximately 0.75 (Figure 4f). This consistent ratio suggests that the differences in crystal morphology observed on the membrane surface arose primarily during the subsequent crystal growth stages, rather than during the initial formation of crystallites in the nucleation phase.

Effects of organic foulants on the surface-mediated gypsum crystallization.

Organic fouling precedes gypsum scaling, altering membrane surface properties (Supplementary Figures 16 and 17), modifying nucleation energy barriers, and influencing crystal growth morphology. It should be noted that the gypsum scaling process under the conditions of Figure 5 involves a superposition of homogeneous nucleation within the concentration polarization (CP) layer and surface-mediated heterogeneous nucleation and adhesion on the membrane. To

isolate and highlight the role of surface-mediated interactions, surface conditioning experiments were conducted under otherwise identical feed composition and hydrodynamic conditions. In brief, the membranes were first pre-treated with solutions containing specific organic foulant, rinsed to form a thin and tightly bound organic layer, and then subjected to pure $CaSO_4$ fouling. The conditioned membrane exhibited a less severe flux decline compared to the fresh membrane when exposed to gypsum scaling (Figure 5a), with HA exhibiting the strongest inhibition (flux decline after 6 h: 15.50% for HA, 55.03% for BSA, and 91.16% for SA). Although homogeneous nucleation in the CP layer is expected to occur simultaneously due to the high supersaturation, the identical feed solution composition and hydrodynamic conditions across all conditioning groups render its contribution a constant baseline. Therefore, the observed differences in flux decline primarily reflect variations in surface-mediated processes, including crystal adhesion and heterogeneous nucleation barriers induced by the different organic conditioning layers. The apparent reversal in inhibition efficiency between Fig. 1a and Fig. 5a reflects a shift in the rate-limiting step from bulk precursor formation to surface attachment, rather than a contradiction in inhibitor functionality. QCM-D analysis revealed distinct adsorption behaviors and nucleation suppression effects (Figure 5b). Both BSA and HA formed rigid interfacial layers ($\Delta D/\Delta f \leq 0.18 \times 10^{-6}$ Hz^{-1}, Figure 5c). BSA primarily suppressed nucleation through steric hindrance, experiencing minimal structural disturbance upon $CaSO_4$ exposure. HA demonstrated the strongest nucleation inhibition (Δf = –14.20 Hz, compared to –68.90 Hz for pure gypsum), with weakened interfacial rigidity, likely due to calcium ion chelation causing the HA layer to loosen around calcium, thereby disrupting nucleation and reducing gypsum adhesion. In contrast, SA formed a gel-like layer that underwent a pronounced structural reorganization upon Ca^{2+} exposure. This transition was evidenced by a shift in $\Delta D/\Delta f$ from 2.35×10^{-6} to 0.89×10^{-6} Hz^{-1}, indicating a transformation from a highly hydrated, soft polymer layer to a more compact and mechanically rigid network. Such behavior is characteristic of calcium-induced ionic cross-linking within alginate chains, consistent with the formation of a hydrogel-type structure rather than a rigid steric barrier.

FIGURE 5.

The adhesion propensity of gypsum was quantified through a comprehensive interfacial energy analysis, integrating surface energy measurements (contact angle, zeta potential;

Supplementary Figure 18) with XDLVO theory calculations. As shown in Figure 5d, the distance-dependent interaction energy profiles highlight three key governing factors: electrostatic (EL) contributions remain negligible due to gypsum's inherently low surface charge, long-range (LW) interactions are consistently attractive across all membrane types, and polar Lewis acid-base (AB) interactions play a dominant role in determining adhesion behavior. BSA conditioning induces a dual effect—while it enhances polar adsorption by shifting AB interactions negatively ($\Delta G_{h_0}^{\mathrm{AB}}$ = –10.24 mJ m^{-2}), it simultaneously reduces LW attraction by 21.5% compared to pristine membranes. In contrast, HA and SA treatments preserve LW interactions but reverse AB polarity through selective modulation of electron donor/acceptor properties, establishing repulsive AB forces ($\Delta G_{h_0}^{\mathrm{AB}}$: +52.20 mJ m^{-2} for HA and +34.53 mJ m^{-2} for SA). These contrasting interfacial interactions result in distinct adhesion thresholds: on BSA-conditioned and pristine membranes, the total energy profile remains negative, facilitating spontaneous gypsum attachment, whereas HA- and SA-conditioned surfaces impose substantial energy barriers of 85.80 and 47.69 kT, respectively, requiring nascent crystals to overcome repulsive forces for surface adhesion. This hierarchical interfacial resistance (HA > SA > BSA) correlates with macroscopic antifouling performance of the conditioned membranes.

A comparison of surface XRD and powder XRD (Supplementary Figure 19) of the fouled membranes confirmed that organic foulants influenced the growth direction of gypsum crystals. BSA inhibited the development of the (020) plane, while HA suppressed growth along the (021) and (041) planes. AFM characterization of crystal faces further revealed distinct differences in step distances and surface textures (Supplementary Note 7). In the presence of BSA, dislocations primarily formed on the crystal surface perpendicular to the *a*-axis, leading to the development of characteristic stepped structures and the formation of short, thick, blocky crystals. In contrast, HA-induced dislocations along the (020) plane resulted in prismatic crystals with scale-like surface patterns.

Spatial dynamics of organic-inorganic mixed fouling.

Synchrotron-based infrared microscopy offers a highly accurate and quantitative approach for *in situ* mapping the spatial distribution of foulants across the membrane surface and within the fouling layer. As schematically illustrated in Figure 6a, the fouled membranes were embedded in paraffin wax, sectioned into thin slices, and fixed onto calcium fluoride (CaF_2) windows. The

measurements were conducted on fouled membranes in transmission mode, enabling spatially resolved two-dimensional scans. After collecting FTIR spectrum on different location (Figure 6b), characteristic peaks of the polyamide membrane (1587 cm^{-1} for N–H bending and C–N stretching), gypsum (3395 cm^{-1} for O–H stretching), and organic foulants (1687 cm^{-1} for BSA amide (I) α-helix, 1012 cm^{-1} for HA O–H deformation, and 1048 cm^{-1} for SA C–O elongation) were extracted and visualized as heatmaps, revealing their spatial distribution and chemical abundance across the membrane surface and fouling layer. Detailed experimental procedures are provided in the Supplementary Information (Supplementary Note 8, Figures 21 and 22).

FIGURE 6.

The spatial distribution and chemical abundance of each foulant on the same membrane sample are presented as a heat map in Figure 6c, and the absorbances of gypsum and organic foulants were plotted against distance from the membrane surface (Figure 6d and Supplementary Figure 23). In the pure gypsum scaling group (Figure 6c_1), gypsum was concentrated near the membrane surface, with its intensity starting to decrease beyond 10 microns from the surface (grey squares in Figure 6d). This decrease corresponds to the effects of concentration polarization, which increases local gypsum supersaturation and promotes crystallization near the membrane. In the BSA group (Figure 6c_2), BSA was detected within 3-4 microns from the membrane surface (blue circles in Figure 6d), without the presence of gypsum, suggesting that BSA adhered to the membrane first. This BSA-rich layer was overlaid by a seven-micron-thick gypsum layer with relatively low intensity. Beyond this, the gypsum layer, another 10-micron-thick BSA layer appeared, indicating that BSA inhibited further gypsum growth. In the HA group (Figure 6c_3), HA was also found on the membrane surface before gypsum. But unlike in the BSA group, HA and gypsum regions overlapped. The highest gypsum abundance was observed about 10 microns away from the membrane surface (orange triangles in Figure 6d), indicating that HA strongly inhibited early-stage gypsum fouling but had a reduced impact on crystal growth in solution. For the SA group (Figure 6c_4), both SA and gypsum signals were low near the membrane surface, which can be attributed to the shrinkage of a highly hydrated alginate gel caused by dehydration during sample preparation. The calcium-cross-linked alginate network (“egg-box” structure) acted as a porous hydrogel layer that temporarily retained calcium ions while altering ion transport pathways near the membrane surface, leading to low gypsum abundance in this region. At greater distances

from the membrane, the spatial distributions of the gypsum and SA overlapped almost completely, indicating that crystal growth occurred within the alginate matrix rather than being excluded by it. Although the maximum gypsum intensity was the lowest in the SA group, the gypsum layer was the thickest, surpassing even the thickness in the pure gypsum group (red diamonds in **Figure 6d**). This result suggests that SA did not effectively suppress overall gypsum growth; instead, the extended gel network provided additional nucleation sites, promoting crystal formation throughout the thickness of the fouling layer.

Correlation analysis between the signal intensities of gypsum and organic foulant at different locations (Figure 6e) revealed that BSA had the lowest correlation with gypsum at 0.22, indicating that their distributions were largely exclusive. BSA, being a large molecule with a low density of surface functional groups, segregated gypsum precursors, preventing their aggregation and crystallization. In contrast, HA and SA showed higher correlations with gypsum, at 0.55 and 0.61, respectively. These smaller molecules, rich in carboxyl functional groups, had less steric hindrance and were able to form clusters or gels with calcium ions, leading to their co-occurrence with gypsum during fouling.

Discussion

Through *in situ* microscopic monitoring, we investigated the homogeneous nucleation and crystallization process within CP layer during membrane desalination under mixed fouling conditions, while separately isolating surface-mediated effects through membrane conditioning experiments. Additionally, we analysed the interfacial interactions between membrane surfaces and gypsum precursor clusters; these analyses revealed distinct mechanisms by which different organic foulants influence gypsum scaling. BSA primarily reduces effective supersaturation during the homogeneous nucleation phase, acting as a “molecular shield” in solution that sterically wraps precursor clusters and kinetically suppresses their growth, and obstructs lateral crystal growth during the final crystallization stage. These combined effects effectively mitigate membrane fouling, resulting in short, thick gypsum crystals with distinct stepped structures. In contrast, HA primarily affects surface-mediated nucleation and functions as a “non-stick interfacial layer” on the membrane surface, which generates strong repulsive hydration and acid–

base interactions that thermodynamically prevent crystal adhesion. This mechanism moderately alleviates gypsum fouling, producing flaky, scale-like crystals with stepped patterns predominantly along the (020) plane. SA, however, exhibits a more uniform effect across all crystallization stages by forming a calcium-cross-linked, gel-like structure consistent with the "egg-box" model, which serves as a porous organic matrix providing gypsum precursor clusters and crystals. While this structure delays the fouling process slightly, it has minimal impact on inhibiting subsequent crystal growth. Instead, crystal growth proceeds within the gel matrix, as evidenced by the high final crystallinity and the rosette-like gypsum crystals embedded in a continuous organic phase observed by SEM. These findings highlight the diverse and stage-specific mechanisms through which organic foulants interact with gypsum during membrane fouling, offering insights into targeted strategies for fouling mitigation in membrane desalination systems.

Observations from previous studies suggest that early-stage gypsum nucleation is not fully captured by classical nucleation descriptions based on ion-by-ion assembly into a crystalline nucleus, and instead may involve the formation of pre-nucleation clusters at initial stages[37,52,58]. Consistent with these reports, our SAXS measurements further indicate that homogeneous gypsum crystallization under RO scaling or mixed fouling conditions proceeds via a precursor-mediated nucleation pathway. Specifically, the process involves the formation of supersaturated solutions containing nanoscale anhydrous $CaSO_4$ precursor clusters, which grow to critical sizes, aggregate, and rearrange into ordered structures with the incorporation of water molecules.

Heterogeneous nucleation at membrane interfaces likewise exhibits behavior that is not fully captured by simplified single-ion attachment descriptions. Some studies suggest that the energy barrier between gypsum and membrane surfaces, influenced by hydrophobicity or hydrophilicity, can in some cases be interpreted within classical heterogeneous nucleation frameworks based on direct ion-by-ion attachment[59,60]. However, contradictory findings indicate scenarios where hydrophilic or hydrophobic surface modifications resulted in fouling tendencies opposite to those predictions[61]. In our study, a similar phenomenon was observed with membranes conditioned by BSA, where increased surface hydrophobicity unexpectedly led to reduced fouling tendencies. Calculations of interaction energy between gypsum precursors and the membrane surface further confirmed that the adhesion of precursor clusters plays a critical role in surface fouling. These

observations suggest that gypsum surface scaling involves a multi-stage, precursor-mediated process comprising precursor formation, aggregation, and rearrangement, which aligns more closely with the Ostwald crystallization rule[21,62].

In summary, by integrating *in situ* high-energy X-ray scattering with synchrotron radiation-based micro-FTIR spectroscopy, this study provides a comprehensive assessment of mixed fouling dynamics in membrane desalination systems. Our findings reveal that mixed fouling is governed by complex interactions between inorganic scaling and organic foulants, with different organic components exerting stage-specific effects on gypsum nucleation and crystallization at distinct interfacial locations. Notably, through analyzing theoretical interaction energy analysis, our study shows that gypsum nucleation in complex aqueous environments cannot be fully described by simplified classical descriptions based solely on single-ion attachment, particularly for both homogeneous and heterogeneous nucleation pathways. Instead, under the conditions examined here, the nucleation process is characterized by the formation of precursor clusters followed by structural reorganization prior to the development of long-range crystalline order, which is consistent with precursor-mediated nucleation scenarios proposed within non-classical frameworks. Beyond establishing an advanced experimental framework for interfacial fouling characterization, this work offers practical guidelines for optimizing membrane operation, designing antifouling surfaces, and improving pretreatment strategies. Collectively, these insights deepen the mechanistic understanding of mixed fouling and pave the way for more effective mitigation strategies in real-world desalination applications.

Methods.

Membrane fouling experiments.

Fouling experiments were conducted in a laboratory-scale reverse osmosis (RO) system with an effective membrane area of 19.5 cm^2 (65 mm × 30 mm). The system temperature was maintained at 25 ± 0.3 ℃ by an industrial chiller (BL-1FCS, Baoli, China). Feed solution contained 30 mM sodium sulfate (Na_2SO_4) and 30 mM calcium chloride ($CaCl_2$), leading to gypsum ($CaSO_4$) concentration of 30 mM. In $CaSO_4$-organic mixed fouling experiments, an additional 100 mg L^{-1} of organic foulant, including bovine serum albumin (BSA), humic acid (HA), and sodium alginate

(SA), was respectively added to the feed solution. Before each fouling experiment, a membrane coupon was compacted with deionized (DI) water at 25 bar for 8 hours, with a crossflow velocity of 30.86 cm s^{-1}. Following the compaction, the crossflow velocity was reduced to 9.26 cm s^{-1}, and the fouling experiment was initiated by sequentially adding sodium sulfate, organic foulant, and calcium chloride stock solutions. Precise hydraulic control was established using a variable frequency pump, which was continuously regulated to maintain the membrane inlet pressure at a consistent value of 25 bar. Concurrently, a constant flow control valve installed on the feed line ensured the cross-flow velocity remained fixed at 30.86 cm s^{-1} throughout the experiment. Under these conditions, the initial water flux achieved was 54 L m^{-2} h^{-1}. Experiment was conducted over a 24-hour period to assess the impact of different feed water compositions on permeate flux. Both the permeate and concentrate streams were continuously recirculated back to the feed tank. To verify experimental reproducibility, replicate fouling experiments were conducted under identical conditions. The resulting individual flux decline curves, presented in Supplementary Figure 4, exhibit a high degree of consistency, confirming the reliability of the experimental results.

Effect of organic foulants on gypsum surface crystallization was evaluated through membrane conditioning and scaling experiments. Membranes were compacted following the same protocol as in the fouling experiments. To initiate the conditioning experiment, 60 mM sodium chloride, 100 mg L^{-1} organic foulants (BSA, HA, or SA), and 30 mM calcium chloride were sequentially added to the feed solution. Sodium sulfate was replaced with an equivalent ionic strength (double the concentration of sodium chloride) to prevent sodium sulfate precipitation. Crossflow velocity and initial flux were maintained as in the fouling experiments, with a conditioning duration of one hour. Then, the membrane underwent backwashing with pure water for 15 minutes to remove ions and loosely adsorbed organic matter. During backwashing, crossflow velocity was 30.86 cm s^{-1}, and the pressure was set to 0.2 bar. Subsequently, a pure gypsum scaling experiment, without adding organic foulants, was conducted under the identical conditions and feed solution composition as in the fouling experiments.

Interaction energy calculated by XDLVO model.

According to extended Derjaguin-Landau-Verwey-Overbeek (XDLVO) theory, the total interaction energy, E_{TOT}, between the foulant and the membrane surface is the sum of three components: electrostatic interaction energy (E_{EL}), Lifshitz-van der Waals interaction energy

(E_{LW}), and Lewis acid-base interaction energy (E_{AB}). At a separation distance h between foulant and membrane interface, the total interaction energy and each of these components can be expressed as:

$$E_{TOT} = E_{LW} + E_{AB} + E_{EL} \quad (1)$$

$$E_{LW}(h) = -\frac{A}{12\pi h^2} \quad (2)$$

$$E_{AB}(h) = \Delta G_{h_0}^{AB} \exp\left(\frac{h_0 - h}{\lambda}\right) \quad (3)$$

$$E_{EL}(h) = \varepsilon_r \varepsilon_0 k \xi_M \xi_F \left[\frac{\xi_M^2 + \xi_F^2}{2\xi_M \xi_F}(1 - \coth kh) + \frac{1}{\sinh kh}\right] \quad (4)$$

where $A = -12\pi h_0^2 \Delta G_{h_0}^{LW}$ represents the Hamaker constant, h_0 is the minimum cutoff distance due to Born repulsion; λ is the characteristic decay constant for polar interactions in aqueous solutions; ε_r is the dielectric constant of water; ε_0 is the permittivity of free space; ξ_1 and ξ_3 denote the surface potentials of the membrane and gypsum, respectively; k is the Debye screening constant, and $1/k$ represents the Debye length, which is 0.104 nm at room temperature. $\Delta G_{h_0}^{LW}$ and $\Delta G_{h_0}^{AB}$ represent the LW and AB components of the Gibbs free energy between surface and foulant at contact, respectively, and are calculated as follows:

$$\Delta G_{MLF,h_0}^{LW} = -2\left(\sqrt{\gamma_M^{LW}} - \sqrt{\gamma_L^{LW}}\right)\left(\sqrt{\gamma_F^{LW}} - \sqrt{\gamma_L^{LW}}\right) \quad (5)$$

$$\Delta G_{MLF,h_0}^{AB} = 2\left[\sqrt{\gamma_L^+}\left(\sqrt{\gamma_M^-} + \sqrt{\gamma_F^-} - \sqrt{\gamma_L^-}\right) + \sqrt{\gamma_L^-}\left(\sqrt{\gamma_M^+} + \sqrt{\gamma_F^+} - \sqrt{\gamma_L^+}\right) - \left(\sqrt{\gamma_M^+\gamma_F^-}\right) + \left(\sqrt{\gamma_M^-\gamma_F^+}\right)\right] \quad (6)$$

where γ^{LW}, γ^+, and γ^-, represent the Lifshitz-van der Waals component of surface energy, and the Lewis acid and Lewis base components, with subscripts L, M, and F representing the liquid, membrane, and gypsum, respectively. The surface energy components of the virgin membrane and the membrane conditioned with organic foulants were determined using the Young-Dupré equation, based on contact angle measurements with three liquids of known surface tension properties (Supplementary Tables 2 and 3):

$$(1+\cos\theta)\left(\gamma_L^{LW}+2\sqrt{\gamma_L^+\gamma_L^-}\right)=2\left(\sqrt{\gamma_S^{LW}\gamma_L^{LW}}+\sqrt{\gamma_S^+\gamma_L^-}+\sqrt{\gamma_L^+\gamma_S^-}\right) \quad (7)$$

Quartz crystal microbalance with dissipation monitoring analysis.

Gold sensors (QSX 301 gold, Nanoscience Instruments, USA) were subjected to a two-step cleaning process. First, the sensors were exposed to UV/ozone (ProCleaner, BioForce Nanosciences, USA) for 10 minutes. Following this, the sensors were immersed in a solution of DI water, ammonia (25%), and hydrogen peroxide (30%) in a 5:1:1 volume ratio at 75 ℃ for 15 minutes. The sensors were then rinsed with DI water, dried using pure, oil-free nitrogen gas, and subjected to a second 10-minute UV/ozone treatment.

Membrane coupons were pretreated with isopropanol and water, then cut into squares slightly larger than the gold sensor. The PET backing layer of the membrane was carefully removed using tweezers, leaving the polysulfone support layer and polyamide functional layer intact. The membrane was then placed on the sensor with the polyamide layer facing the sensor surface, and secured with a glass slide and binder clip. To dissolve the polysulfone layer, DMF was added dropwise onto the membrane surface in a 65 ℃ forced-air drying oven until dissolution was complete. The sensor was then annealed at 65 ℃ for five minutes to ensure thorough drying, leaving only the polyamide layer adhered to the surface.

Mass accumulation of foulants on the sensor was measured using quartz crystal microbalance with dissipation monitoring (QCM-D, QSense Explorer, Biolin Scientific, Sweden). The mass change and frequency change detected by the sensor can be described by the Sauerbrey equation:

$$\Delta f = -\frac{2 f_0^2}{A\sqrt{\rho_q \mu_q}}\Delta m \quad (8)$$

where Δf is the frequency change, f_0 is the resonant frequency of the fundamental mode, *A is the* piezoelectrically active crystal area, ρ_q is the density of quartz, μ_q is the shear modulus of quartz for the AT-cut crystal, and Δm is the mass change on the sensor.

Since the same polyamide-coated sensor was used in all experiments, sensor-related parameters were assumed to remain consistent. Therefore, the mass of the foulants deposited on the sensor (Δm) was directly inferred by the frequency change (Δf). Before each test, the

polyamide-coated sensor was installed in a flow chamber, where DI water was circulated for at least four hours to stabilize the frequency (*f*-value) with a drift of less than 0.1 Hz min^{-1}.

To establish a baseline, pure water was initially introduced, followed by addition of 100 mM sodium chloride to further stabilize the baseline. For the pure gypsum group, a 50 mM gypsum solution (composed of 50 mM calcium chloride and 50 mM sodium sulfate) was subsequently added. For the organic foulant conditioning groups, a solution containing 100 mg L^{-1} of either BSA, HA, or SA was introduced, along with 10 mM magnesium chloride as a divalent ion to simulate the effects of calcium on organic foulants, and 80 mM sodium chloride to maintain ionic strength. After a 30-minute exposure to the organic foulant solution, the system was switched back to 100 mM sodium chloride to rinse away any loosely adsorbed foulants. Once the signal stabilized, a 50 mM gypsum solution was introduced. All QCM-D experiments were performed at 25 ℃, with a flow rate of 100 μL min^{-1}.

Operating protocol for synchrotron infrared mapping.

Synchrotron infrared spectra were collected at the National Synchrotron Radiation Laboratory (NSRL, Hefei, China) on the Beamline of Infrared Spectroscopy and Microspectroscopy (BL01B). Infrared radiation was sourced from a bending magnet with an acceptance angle of 65(H) × 55(V) $mrad^2$, capturing both edge and constant field radiation[63]. The setup includes a Bruker IFS 66v Fourier transform spectrometer and a Bruker Hyperion 3000 microscope, with infrared imaging conducted in transmission mode employing a spectral resolution of 4 cm^{-1} over the 700–8000 cm^{-1} range, and a mapping step size of 4 μm (with a diffraction-limited spot size of ~10 μm at 1000 cm^{-1}) to achieve high spatial and spectral resolution. The synchrotron IR measurements were conducted on fouled membranes collected from the membrane fouling experiments (corresponding to the conditions shown in Figure 1). Sliced samples were positioned on a motorized *x*-*y* stage, and background spectra were recorded from the CaF_2 window (Figure 1a). Sample cross-section structure, including both the membrane and the fouling layer on top, was identified under an optical microscope, and spectral mapping was performed covering a 10 × 40-pixel area with a step size of 4 microns. Each pixel was scanned 64 times. The mapping data were processed using OPUS software (Version 7.5, Bruker, Germany).

Simulation of concentration polarization layer.

The concentration of solute at the membrane surface (c_m) is described by:

$$\frac{c_m - c_p}{c_b - c_p} = \exp(\frac{J\delta}{D}) = \exp(\frac{J}{k}) \quad (9)$$

where c_m represents the concentration of the substance at the membrane surface, c_b is the solute concentration in the bulk solution, c_p is the concentration in the permeate, J is the water flux, δ is the thickness of the concentration polarization layer, D is the diffusion coefficient of the substance in water, and k is the kinematic viscosity.

Assuming complete retention of divalent ions and organic molecules by the BW30 membrane, the concentration at the permeate side (c_p) is considered to be zero. The mass transfer coefficient (k) can be calculated by:

$$k = \frac{D \cdot Sh}{d_h} = 1.85 \frac{D}{d_h} (\frac{Re \cdot Sc \cdot d_h}{\text{Channel Length}})^{\frac{1}{3}} \quad (10)$$

where Sh is the Sherwood number, d_h is the wetted perimeter related to membrane module's dimensions, Re is the Reynolds number, and Sc is the Schmidt number.

The thickness of the concentration polarization layer (δ) for each solute at the membrane surface is related to its diffusion coefficient (D) in water, while the kinematic viscosity (k) depends on the solute concentration in the feed solution. Other parameters, associated with membrane cell dimensions and operating conditions, remain consistent across all experiments. Therefore, the concentration of a substance at any position within the concentration polarization layer can be calculated by:

$$c = c_b \cdot \exp(\frac{J(\delta - x)}{D}) \quad (11)$$

where x is the distance from the membrane surface. Details of the calculation of wetted perimeter (d_h), Sherwood number (Sh), Reynolds number (Re), crossflow velocity (Q and u), kinematic viscosity (k), and Schmidt number (Sc), are provided in the Supplementary Information (Supplementary Note 2).

Procedures for synchrotron X-ray scattering/diffraction measurements.

Sample preparation. The simulated concentration polarization layer solutions were prepared based on the calculated membrane surface concentration (c_m), with the concentration of each component

in each solution group detailed in Table 1. The pure gypsum group was created by mixing equal volumes of $CaCl_2 \cdot 2H_2O$ and Na_2SO_4 solutions. For the gypsum-organic mixture groups, the organic foulant was first mixed with the Na_2SO_4 solution, and pH was adjusted to 7 before mixing with the $CaCl_2$ solution. For BSA, since the calculated c_m concentration was too high, we reduced it to 1/20 of the original value during preparation. The saturation index (SI) of the solutions was calculated using Visual MINTEQ software (version 3.1), with an SI greater than zero under the specified physicochemical conditions indicating that the mixed solution was supersaturated with respect to gypsum (Supplementary Note 2).

Table 1. Salt and organic foulant concentrations in the simulated concentration polarization layer solutions for each group.

Feed solute compounds	$[CaCl_2]$ (mM)	$[Na_2SO_4]$ (mM)	Organic Foulant (g L^{-1})
Gypsum only	136.66	104.15	N.A.
Gypsum + BSA	136.66	104.15	BSA (23.83)
Gypsum + HA	136.66	104.15	HA (3.73)
Gypsum + SA	136.66	104.15	SA (0.47)

In situ device set up. The induction time was determined by in situ, time-resolved synchrotron SAXS/WAXS measurements, in which the simulated concentration polarization layer solution was reacted under well-mixed, flow-controlled conditions. Specifically, 100 mL of Na_2SO_4 (or mixture solution of Na_2SO_4 and organic foulant) was first added to a 250 mL polypropylene beaker, continuously stirred at 500 rpm, and circulated through a quartz capillary (Φ1.86/φ 1.46, Hirschmann, German) on the sample holder using a peristaltic pump at a flow rate of 10 mL min^{-1}. This flow rate corresponds to a crossflow velocity of 9.96 cm s^{-1}, which is largely comparable to the 9.26 cm s^{-1} crossflow velocity used in the laboratory-scale RO fouling experiments, thereby ensuring that the hydrodynamic shear conditions are well-aligned with those near the membrane surface. A remote-controlled syringe pump was then used to rapidly inject 100 mL of $CaCl_2$ solution into the beaker within 30 seconds to initiate the scaling. The experiment lasted for forty minutes, during which the synchrotron X-ray beam was directed through the quartz capillary, continuously collecting scattering patterns, with each exposure lasting five seconds. *In situ* SAXS/WAXS measurements were performed under a highly stable ambient temperature of 25 °C at the beamline, with continuous monitoring in replicate experiments confirming a minimal reaction temperature variation of ± 0.3 °C, ensuring thermal stability. It should be emphasized that

no membrane substrate was involved in this in situ SAXS/WAXS setup; the capillary-based configuration was solely designed to probe homogeneous crystallization kinetics within the simulated concentration polarization solution.

Scattering Protocol. In situ time-resolved ultra-small-angle X-ray scattering (USAXS) was conducted on the Time-Resolved Ultra-Small-Angle X-ray Scattering Beamline (BL10U1) at the Shanghai Synchrotron Radiation Facility (SSRF, Shanghai, China)[64]. A monochromatic X-ray beam with an energy of 10 keV (1.24 Å) was used, and scattering intensity at ultra-small angles was recorded by an Eiger 4M detector. Calibration was conducted using dry collagen as the standard, with a sample-to-detector distance of 27 m, yielding a scattering vector, q, in a range of $0.0125 < q < 0.2$ nm^{-1}.

Small-angle X-ray scattering (SAXS) and wide-angle X-ray scattering (WAXS) measurements were performed at the Biological Small Angle X-ray Scattering Beamline (BL19U2)[36] at SSRF. The X-ray beam energy was 12 keV (1.033 Å). SAXS data were collected using a Pilatus 2M detector, calibrated with a silver behenate standard, with a sample-to-detector distance of 2.725 m, covering a q range of $0.08 < q < 4$ nm^{-1}. WAXS data were collected using a Pilatus 300kW detector, calibrated using a highly crystalline silicon standard, with a sample-to-detector distance of 0.213 m, covering a q range of $4.5 < q < 50$ nm^{-1}. The SAXS and WAXS detectors were synchronized to ensure that each frame in SAXS corresponds directly to the same frame in WAXS. Scattering data were corrected for absolute intensity using water as the standard[65].

Data processing. In all datasets from each group of samples, the scattering patterns were circular and independent of the azimuthal angle in the detector plane, indicating an isotropic system. As a result, the two-dimensional patterns were directly integrated over the scattering vector q to produce one-dimensional curves. USAXS data processing included several steps: detector calibration, masking of the beamstop and detector gap, background subtraction, and azimuthal integration, all performed using the Data Analysis WorkbeNch (DAWN) software package (Version 2.28, Diamond Light Source, UK)[66]. In the Guinier region ($qR_G < 1.3$), the radius of gyration (R_G) was calculated using the Guinier Law:

$$\ln\left[I(q)\right] \cong -\frac{q^2 R_G^2}{3} + \ln\left[I(0)\right] \tag{12}$$

where q is the scattering vector, defined as $q = (4\pi/\lambda)\sin(\theta)$, where λ is the wavelength of the X-ray, and 2θ is the scattering angle. $I(q)$ represents the scattering intensity at a given scattering vector q, $I(0)$ is the intensity extrapolated to zero angle, and R_G is the radius of gyration of the scatterers.

SAXS data were processed using BioXTAS RAW software (Version 2.2.1)[67], with absolute intensity correction using water before integration. After generating one-dimensional curves, profile comparison with residuals was performed. WAXS data were calibrated and integrated using pyFAI (Version 2023.9)[68]. The induction time t_{ind} of crystallization was defined by the following equation: $t_{ind} = t_{obs} - t_0$, where t_{obs} is the elapsed time until the first detectable appearance of the characteristic gypsum (020) diffraction peak in the time-resolved WAXS frames, and t_0 represents the time of initial supersaturation (i.e., $CaCl_2$ injection). The gypsum crystallinity (α) at a specific time was calculated by normalizing the peak area of the gypsum (020) peak reflection to the maximum peak area observed in the pure gypsum group. The average grain size in the direction perpendicular to the (020) plane was calculated using the Scherrer equation:

$$\tau = \frac{K\lambda}{\beta \cos\theta} \tag{13}$$

where τ represents the average crystallite size; K is the Scherrer constant (shape factor) set to 1; β denotes the full width at half maximum (FWHM) of the (020) peak, and θ is the Bragg angle corresponding to that peak. Due to the uneven growth of polycrystals, the average crystal grain size is capped at 8 nm to ensure it falls within the applicable range of the Scherrer equation.

Statistics & Reproducibility.

All key experiments, including membrane fouling runs and *in situ* synchrotron X-ray scattering measurements, were performed in at least triplicate to ensure the reproducibility of our findings. Consistent trends across independent replicates are provided in the Supplementary Information (Supplementary Figures 4 and 7).

Data Availability

The data supporting the findings of the study are included in the main text and supplementary information files. Source data are provided with this paper.

References.

1 Nancollas, G. & Reddy, M. The kinetics of crystallization of scale-forming minerals. *Society of Petroleum Engineers Journal* **14**, 117-126 (1974).

2 Bottrell, S. H. & Newton, R. J. Reconstruction of changes in global sulfur cycling from marine sulfate isotopes. *Earth-Science Reviews* **75**, 59-83 (2006).

3 Fouke, B. W. *et al.* Depositional facies and aqueous-solid geochemistry of travertine-depositing hot springs (Angel Terrace, Mammoth Hot Springs, Yellowstone National Park, USA). *Journal of Sedimentary Research* **70**, 565-585 (2000).

4 Elimelech, M. & Phillip, W. A. The future of seawater desalination: energy, technology, and the environment. *science* **333**, 712-717 (2011).

5 Ahmed, M. A., Amin, S. & Mohamed, A. A. Fouling in reverse osmosis membranes: monitoring, characterization, mitigation strategies and future directions. *Heliyon* **9** (2023).

6 McCutcheon, J. R. & Mauter, M. S. Fixing the desalination membrane pipeline. *Science* **380**, 242-244 (2023).

7 Løge, I. A., Anabaraonye, B. U. & Fosbøl, P. L. Growth mechanisms of composite fouling: The impact of substrates on detachment processes. *Chemical Engineering Journal* **446**, 137008 (2022).

8 Cai, Y.-H., Burkhardt, C. J. & Schäfer, A. I. Renewable energy powered membrane technology: Impact of osmotic backwash on organic fouling during solar irradiance fluctuation. *Journal of Membrane Science* **647**, 120286 (2022).

9 Ennaceri, H., Fischer, K., Schulze, A. & Moheimani, N. R. Membrane fouling control for sustainable microalgal biodiesel production: A review. *Renewable and Sustainable Energy Reviews* **161**, 112335 (2022).

10 Cruz, C., Cisternas, L. A. & Kraslawski, A. Scaling problems and control technologies in industrial operations: Technology Assessment. *Separation and Purification Technology* **207**, 20-27 (2018).

11 Meng, J. & Wang, S. Advanced antiscaling interfacial materials toward highly efficient heat energy transfer. *Advanced Functional Materials* **30**, 1904796 (2020).

12 Jafari, M. *et al.* Cost of fouling in full-scale reverse osmosis and nanofiltration installations in the Netherlands. *Desalination* **500**, 114865 (2021).

13 Van de Lisdonk, C., Van Paassen, J. & Schippers, J. Monitoring scaling in nanofiltration and reverse osmosis membrane systems. *Desalination* **132**, 101-108 (2000).

14 Li, W. *et al.* Application of high-dose UV irradiation as nanofiltration pretreatment for drinking water production: Organic fouling mitigation and micropollutant removal. *Water Research* **266**, 122348 (2024).

15 Khan, I. A., Lee, Y. S. & Kim, J.-O. Chemically enhanced pretreatment (CEPT) to reduce irreversible fouling during the clean-in-place process for membranes operating under constant flux and constant pressure filtration. *Desalination* **549**, 116313 (2023).

16 Yin, Y. *et al.* The use of anti-scalants in gypsum scaling mitigation: Comparison with membrane surface modification and efficiency in combined reverse osmosis and membrane distillation. *Journal of Membrane Science* **643**, 120077 (2022).

17 Hsieh, I.-M. & Malmali, M. Scaling behavior in membrane distillation: Effect of Biopolymers and Antiscalants. *Water Research* **255**, 121456 (2024).

18 Gibbs, J. W. On the equilibrium of heterogeneous substances. *American Journal of Science* **3**, 441-458 (1878).

19 Lee, J., Yang, J., Kwon, S. G. & Hyeon, T. Nonclassical nucleation and growth of inorganic nanoparticles. *Nature Reviews Materials* **1**, 1-16 (2016).

20 Van Driessche, A. E., Kellermeier, M., Benning, L. G. & Gebauer, D. in *New Perspectives on Mineral Nucleation and Growth* (Springer, 2017).

21 Gebauer, D. & Cölfen, H. Prenucleation clusters and non-classical nucleation. *Nano Today* **6**, 564-584 (2011).

22 Hoang, T. A. in *Water-formed deposits* 13-47 (Elsevier, 2022).

23 Anklam, M. R. & Firoozabadi, A. An interfacial energy mechanism for the complete inhibition of crystal growth by inhibitor adsorption. *The Journal of chemical physics* **123** (2005).

24 Lin, D. *et al.* Nanofiltration scaling influenced by coexisting pollutants considering the interaction between ferric coagulant and natural organic macromolecules. *Chemical Engineering Journal* **413**, 127403, (2021).

25 Jermann, D., Pronk, W. & Boller, M. Mutual influences between natural organic matter and inorganic particles and their combined effect on ultrafiltration membrane fouling. *Environmental science & technology* **42**, 9129-9136 (2008).

26 Ji, J., Qiu, J., Wai, N., Wong, F.-S. & Li, Y. Influence of organic and inorganic flocculants on physical–chemical properties of biomass and membrane-fouling rate. *Water research* **44**, 1627-1635 (2010).

27 Quay, A. N. *et al.* Combined organic fouling and inorganic scaling in reverse osmosis: role of protein–silica interactions. *Environmental science & technology* **52**, 9145-9153 (2018).

28 Zhang, Y. *et al.* Inhibition of crystal nucleation and growth: a review. *Crystal Growth & Design* **24**, 2645-2665 (2024).

29 Jin, B., Liu, Z. & Tang, R. Recent experimental explorations of non-classical nucleation. *CrystEngComm* **22**, 4057-4073 (2020).

30 Zang, S. *et al.* Direct observation and control of non-classical crystallization pathways in binary colloidal systems. *Nature Communications* **16**, 3645 (2025).

31 Fenter, P. A., Rivers, M. L., Sturchio, N. & Sutton, S. R. *Applications of synchrotron radiation in low-temperature geochemistry and environmental science*. Vol. 49 (Walter de Gruyter GmbH & Co KG, 2018).

32 Liu, Y. *et al.* Progress and challenges in structural, in situ and operando characterization of single-atom catalysts by X-ray based synchrotron radiation techniques. *Chemical Society Reviews* (2024).

33 Deng, N. *et al.* Selenite and selenate sequestration during coprecipitation with barite: insights from mineralization processes of adsorption, nucleation, and growth. *Environmental Science & Technology* **56**, 15518-15527 (2022).

34 Stawski, T. M. *et al.* Formation of calcium sulfate through the aggregation of sub-3 nanometre primary species. *Nature Communications* **7**, 11177 (2016).

35 Pauw, B. R. Everything SAXS: small-angle scattering pattern collection and correction. *Journal of Physics: Condensed Matter* **25**, 383201 (2013).

36 Li, Y.-W. *et al.* BL19U2: Small-angle X-ray scattering beamline for biological macromolecules in solution at SSRF. *Nuclear Science and Techniques* **31**, 117 (2020).

37 Bishnoi, A., Kumar, S. & Joshi, N. in *Microscopy methods in nanomaterials characterization* 313-337 (Elsevier, 2017).

38 Toso, S., Baranov, D., Giannini, C., Marras, S. & Manna, L. Wide-angle x-ray diffraction evidence of structural coherence in CsPbBr3 nanocrystal superlattices. *ACS materials letters* **1**, 272-276 (2019).

39 Yang, Z. *et al.* Visualization and semiquantitative study of the distribution of major components in wheat straw in mesoscopic scale using fourier transform infrared microspectroscopic imaging. *Analytical chemistry* **90**, 7332-7340 (2018).

40 Luo, W., Arhatari, B., Gray, S. R. & Xie, M. Seeing is believing: Insights from synchrotron infrared mapping for membrane fouling in osmotic membrane bioreactors. *Water research* **137**, 355-361 (2018).

41 Xie, M., Luo, W. & Gray, S. R. Synchrotron Fourier transform infrared mapping: A novel approach for membrane fouling characterization. *Water research* **111**, 375-381 (2017).

42 Li, S. *et al.* Synchrotron FTIR mapping of mineralization in a microfluidic device. *Lab on a Chip* **17**, 1616-1624 (2017).

43 He, S., Oddo, J. E. & Tomson, M. B. The inhibition of gypsum and barite nucleation in NaCl brines at temperatures from 25 to 90°C. *Applied Geochemistry* **9**, 561-567 (1994).

44 Huang, X., Li, C., Zuo, K. & Li, Q. Predominant Effect of Material Surface Hydrophobicity on Gypsum Scale Formation. *Environmental Science & Technology* **54**, 15395-15404 (2020).

45 Dai, Z. *et al.* Gypsum scale formation and inhibition kinetics with implications in membrane system. *Water Res* **225**, 119166 (2022).

46 Liu, S. & Nancollas, G. A kinetic and morphological study of the seeded growth of calcium sulfate dihydrate in the presence of additives. *Journal of Colloid and Interface Science* **52**, 593-601 (1975).

47 Cao, T., Rolf, J., Wang, Z., Violet, C. & Elimelech, M. Distinct impacts of natural organic matter and colloidal particles on gypsum crystallization. *Water Research* **218**, 118500 (2022).

48 Cody, A. & Cody, R. Evidence for micro-biological induction of {101} montmartre twinning of gypsum (CaSO4·· 2H2O). *Journal of crystal growth* **98**, 721-730 (1989).

49 Cody, A. & Cody, R. SEM and polarization analyzes updating early light microscope studies related to {101} twin formation in gypsum. *Journal of crystal growth* **98**, 731-738 (1989).

50 He, S., Oddo, J. E. & Tomson, M. B. The nucleation kinetics of calcium sulfate dihydrate in NaCl solutions up to 6 m and 90 C. *Journal of colloid and interface science* **162**, 297-303 (1994).

51 Choi, J. Y., Lee, T., Cheng, Y. & Cohen, Y. Observed crystallization induction time in seeded gypsum crystallization. *Industrial & Engineering Chemistry Research* **58**, 23359-23365 (2019).

52 Van Driessche, A. *et al.* The role and implications of bassanite as a stable precursor phase to gypsum precipitation. *science* **336**, 69-72 (2012).

53 Wang, Y.-W., Kim, Y.-Y., Christenson, H. K. & Meldrum, F. C. A new precipitation pathway for calcium sulfate dihydrate (gypsum) via amorphous and hemihydrate intermediates. *Chemical Communications* **48**, 504-506 (2012).

54 Prosa, T. J., Bauer, B. J., Amis, E. J., Tomalia, D. A. & Scherrenberg, R. A SAXS study of the internal structure of dendritic polymer systems. *Journal of Polymer Science Part B: Polymer Physics* **35**, 2913-2924 (1997).

55 Konishi, T. *et al.* Origin of SAXS intensity in the low-q region during the early stage of polymer crystallization from both the melt and glassy state. *Physical Review Materials* **2**, 105602 (2018).

56 de Moor, P.-P. E., Beelen, T. P. & van Santen, R. A. SAXS/WAXS study on the formation of precursors and crystallization of silicalite. *Microporous materials* **9**, 117-130 (1997).

57 Rabizadeh, T., Stawski, T. M., Morgan, D. J., Peacock, C. L. & Benning, L. G. The effects of inorganic additives on the nucleation and growth kinetics of calcium sulfate dihydrate crystals. *Crystal Growth & Design* **17**, 582-589 (2017).

58 Saha, A. *et al.* New Insights into the transformation of calcium sulfate hemihydrate to gypsum using time-resolved cryogenic transmission electron microscopy. *Langmuir* **28**, 11182-11187 (2012).

59 Tong, T., Wallace, A. F., Zhao, S. & Wang, Z. Mineral scaling in membrane desalination: Mechanisms, mitigation strategies, and feasibility of scaling-resistant membranes. *Journal of membrane science* **579**, 52-69 (2019).

60 Horseman, T. *et al.* Wetting, scaling, and fouling in membrane distillation: state-of-the-art insights on fundamental mechanisms and mitigation strategies. *ACS ES&T Engineering* **1**, 117-140 (2020).

61 Yin, Y. *et al.* Which surface is more scaling resistant? A closer look at nucleation theories for heterogeneous gypsum nucleation in aqueous solutions. *Environmental Science & Technology* **56**, 16315-16324 (2022).

62 Van Santen, R. The Ostwald step rule. *The Journal of Physical Chemistry* **88**, 5768-5769 (1984).

63 Hu, C., Wang, X., Qi, Z. & Li, C. The new infrared beamline at NSRL. *Infrared Physics & Technology* **105**, 103200, (2020).

64 Hua, W.-Q. *et al.* Time-resolved ultra-small-angle X-ray scattering beamline (BL10U1) at SSRF. *Nuclear Science and Techniques* **35**, 36 (2024).

65 Zeng, J. *et al.* Performance on absolute scattering intensity calibration and protein molecular weight determination at BL16B1, a dedicated SAXS beamline at SSRF. *Journal of Synchrotron Radiation* **24**, 509-520 (2017).

66 Basham, M. *et al.* Data analysis workbench (DAWN). *Journal of synchrotron radiation* **22**, 853-858 (2015).

67 Hopkins, J. B., Gillilan, R. E. & Skou, S. BioXTAS RAW: improvements to a free open-source program for small-angle X-ray scattering data reduction and analysis. *Journal of applied crystallography* **50**, 1545-1553 (2017).

68 Ashiotis, G. *et al.* The fast azimuthal integration Python library: pyFAI. *Journal of applied crystallography* **48**, 510-519 (2015).

Acknowledgments.

We gratefully acknowledge the financial support from the National Science Foundation of China (52170094 and 22576197 to X.L.) and the Fundamental Research Funds for the Central Universities (to X.L). We thank the National Facility for Protein Science in Shanghai of BL19U2 (https://cstr.cn/31129.02.NFPS.BL19U2) for providing technical support and assistance in SAXS/WAXS measurements. We also thank the Shanghai Synchrotron Radiation Facility of BL10U1 (https://cstr.cn/31124.02.SSRF.BL10U1) and BL16B1 (https://cstr.cn/31124.02.SSRF.BL16B1) for the assistance on USAXS/SAXS/WAXS measurements. We thank the National Synchrotron Radiation Laboratory of BL01B (https://cstr.cn/31131.02.HLS.IRSM) for the assistance on infrared mapping measurements. Some material characterization was carried out at the University of Science and Technology of China (USTC) Center for Micro- and Nanoscale Research and Fabrication, the Instruments Center for Physical Science at USTC, and the First Affiliated Hospital of USTC. We are grateful to Qingbo Xu at USTC for his assistance with the detector calibration for SAXS and WAXS measurements.

Author Contributions

X.L. conceived the idea. Z.F. and X.L designed experiments. Z.F., S.X., and Z.R. performed experiments. J.C. conducted crystallographic analysis. Z.F., S.X., J.C., Y.Y., J.J., X.F., and X.L. contributed to the data interpretation. Z.F., Z.R., and X.L. wrote the first draft. X.L., Z.F., S.X., and Y.Y. revised the masnuscript. All the authors discussed the results.

Competing Interests

The authors declare that they have no competing interests.

Figure Legends.

Figure 1. The fluxes in the gypsum contamination groups as a function of operation time under the influence of (a) BSA, (b) HA, (c) SA. The symbols in the figure legend represent different feed solutions containments, with triangles in all three plots represent the same pure gypsum scaling control group, indicating 30 mM $CaCl_2$ and 30 mM Na_2SO_4, squares indicating 30 mM $CaCl_2$, 30 mM Na_2SO_4, and 100 mg L^{-1} organic foulant, and circles indicating 30 mM $CaCl_2$ and 100 mg L^{-1} organic foulant. The fouling conditions were as follows: the solution pH was adjusted to 7.0 ± 0.4, with an initial water flux of 54 L m^{-2} h^{-1}. The crossflow velocity within the membrane cell was maintained at 9.26 cm s^{-1}, and the temperature was consistently held at 25.0 ± 0.3 °C. (d) Scanning electron microscopy (SEM) images of the fouled membrane surfaces. (e) High-magnification SEM images of gypsum crystal morphology with schematic diagrams of the corresponding crystal faces.

Figure 2. Schematic of concentration polarization phenomenon and in situ SAXS/WAXS setup. (a) Schematic diagram of gypsum scaling during the reverse osmosis membrane process. (b) Calcium sulfate concentration as a function of distance to membrane surface. (c_1) Experimental setup employed in synchrotron facility. Sodium sulfate or a mixed solution of sodium sulfate and organic foulant is placed in a beaker, and a syringe pump injects calcium chloride solution into the beaker to initiate the reaction. The reaction solution is passed through a quartz capillary at a controlled flow rate using a peristaltic pump, and X-rays irradiate the quartz capillary to collect scattered signals. (c_2) The WAXS and SAXS detectors were positioned at 2.735 m and 0.198 m from the sample, respectively, with continuous exposure, capturing one frame every 5 seconds. The two detectors were precisely synchronized to ensure simultaneous data acquisition.

Figure 3. Time-resolved SAXS analysis of calcium sulfate nucleation under concentration polarization. (a) Time-resolved USAXS patterns during $CaSO_4$ precipitation in the simulated concentration polarization layer from: 85 mM $CaSO_4$ solution, an 85 mM $CaSO_4$ solution with 2325.06 mg L^{-1} BSA, an 85 mM $CaSO_4$ solution with 151.28 mg L^{-1} HA, and an 85 mM $CaSO_4$ solution with 158.30 mg L^{-1} SA. The transitions between phases are marked by dashed lines and indicated by arrows: the blue dashed lines separate the first and second phases, the yellow dashed lines mark the growth phase of the third phases, and the red dashed lines indicate the beginning of the fourth phases. SAXS patterns of pure $CaSO_4$ group in (b) the first 120 s and (c) between 400 s and 1800 s, the arrow points to the part of the curve affected by the form factor. Schematic representation the formation, growth, and aggregation of primary species during the early stage of gypsum crystallization. (d) Progressive change in the intensities in the SAXS patterns in the first 400 s. (e) The radius of gyration of the scatterers in the four sample as a function of time.

Figure 4. Time-resolved WAXS investigation of crystallization pathways and structural evolution dynamics during gypsum formation under concentration polarization. (a) Time-resolved WAXS patterns during gypsum precipitation in the simulated concentration polarization layer from: 85 mM $CaSO_4$ solution, an 85 mM $CaSO_4$ solution with 2325.06 mg L^{-1} BSA, an 85 mM $CaSO_4$ solution with 151.28 mg L^{-1} HA, and an 85 mM $CaSO_4$ solution with 158.30 mg L^{-1} SA. The arrows indicate the primary characteristic peaks of the gypsum crystal: (020), (021), and (041). (b) The BSA group was used as an example. The evolution of the WAXS patterns reflects the stages of crystal formation and growth in gypsum following nucleation. (c) Degree of crystallization versus time from the corresponding WAXS measurements derived from the change in the area of the (020). (d) Induction times for gypsum formation, for pure and organic additive containing solutions. The schematic diagram of (e_1) the calculation of crystallite size for specific crystal

planes and (e_2) the (020) and (021) planes of the gypsum crystal. (f) Crystallite size in the direction perpendicular to the (020) lattice plane and the intensity ratio between the (020) and (021) crystal planes at the end of the reaction. Error bars indicate the standard deviation of the mean (n = 3).

Figure 5. Surface-mediated gypsum nucleation and crystallization on conditioned membrane surface. (a) Flux decline trends during organic conditioning and subsequent pure gypsum fouling process. The fouling protocol included conditioning for 1 hour with a solution of 60 mM sodium chloride, 30 mM calcium chloride, and 100 mg L^{-1} of organic foulant, with an initial water flux of 81 L m^{-2} h^{-1} and a crossflow velocity of 9.26 cm s^{-1}. This procedure was followed by a 15-minute rinse at three times the crossflow velocity. The fouling phase then continued for 6 hours with a solution of 30 mM calcium chloride and 30 mM sodium sulfate, following the same protocol as the mixed fouling process. (b) Time-dependent changes in deposition frequency (Δf) observed in QCM-D experiments for gypsum adsorption following organic conditioning. The mobile phase composition was as follows: Stage I and Stage III used 100 mM NaCl, Stage II included 100 mg L^{-1} of BSA/HA/SA with 10 mM $MgCl_2$ and 80 mM NaCl, and Stage IV contained 50 mM $CaCl_2$ with 50 mM Na_2SO_4. (c) Calculated $\Delta D/\Delta f$ values at adsorption equilibrium during Stages II and IV, illustrating the structural differences in adsorption layers formed by various organic foulants. Data points represent the mean of three independent runs, with error bars denoting the standard deviation (n = 3). (d) Distribution of interaction energy as a function of distance between gypsum and both virgin and conditioned membranes: (1) virgin membrane, (2) BSA-conditioned membrane, (3) HA-conditioned membrane, and (4) SA-conditioned membrane. The inflection point on the total energy curve (grey line) indicates the energy barrier.

Figure 6. Spatial foulant distribution of membrane cross-sections revealed by synchrotron radiation infrared microscopy. (a) Schematic diagram of synchrotron radiation microscopic infrared mapping of membrane cross-section. The fouled membrane was embedded in paraffin, sliced, loaded on a calcium fluoride window, and placed on a two-dimensional translation microstage for microscopic infrared testing. (b) The BSA group was used as an example. A rectangular area is selected on the cross-sectional sample, where simultaneous infrared measurements are conducted on 10 × 40 points in transmission mode, with a step size of 4 μm in both the horizontal and vertical directions. The integrated area of each spectral peak is calculated, and the results are plotted as a heatmap corresponding to their positions, thereby generating a profile map of the membrane or foulant. (c) Synchrotron IR Mapping of Scaling Layer Cross-Sections: (c_1) Pure Gypsum, (c_2) Gypsum + BSA, (c_3) Gypsum + HA, (c_4) Gypsum + SA. The horizontal axis scale was the relative length from fouling layer to membrane interface. (d) Quantitative analyses of gypsum abundance, the absorbance of gypsum was plotted against composition. (e) Correlation between the signal strengths of organic foulants and gypsum fouling.

Editorial Summary:

Scaling is a major challenge in engineered systems. This study employs in situ synchrotron X-ray scattering to reveal how organic matter alters nucleation and crystallization pathways, thereby regulating gypsum scaling on desalination membranes.

Peer review information: *Nature Communications* thanks Wenhai Luo, Yuelian Peng, Zhengyang Huo and the other, anonymous, reviewer(s) for their contribution to the peer review of this work. A peer review file is available.

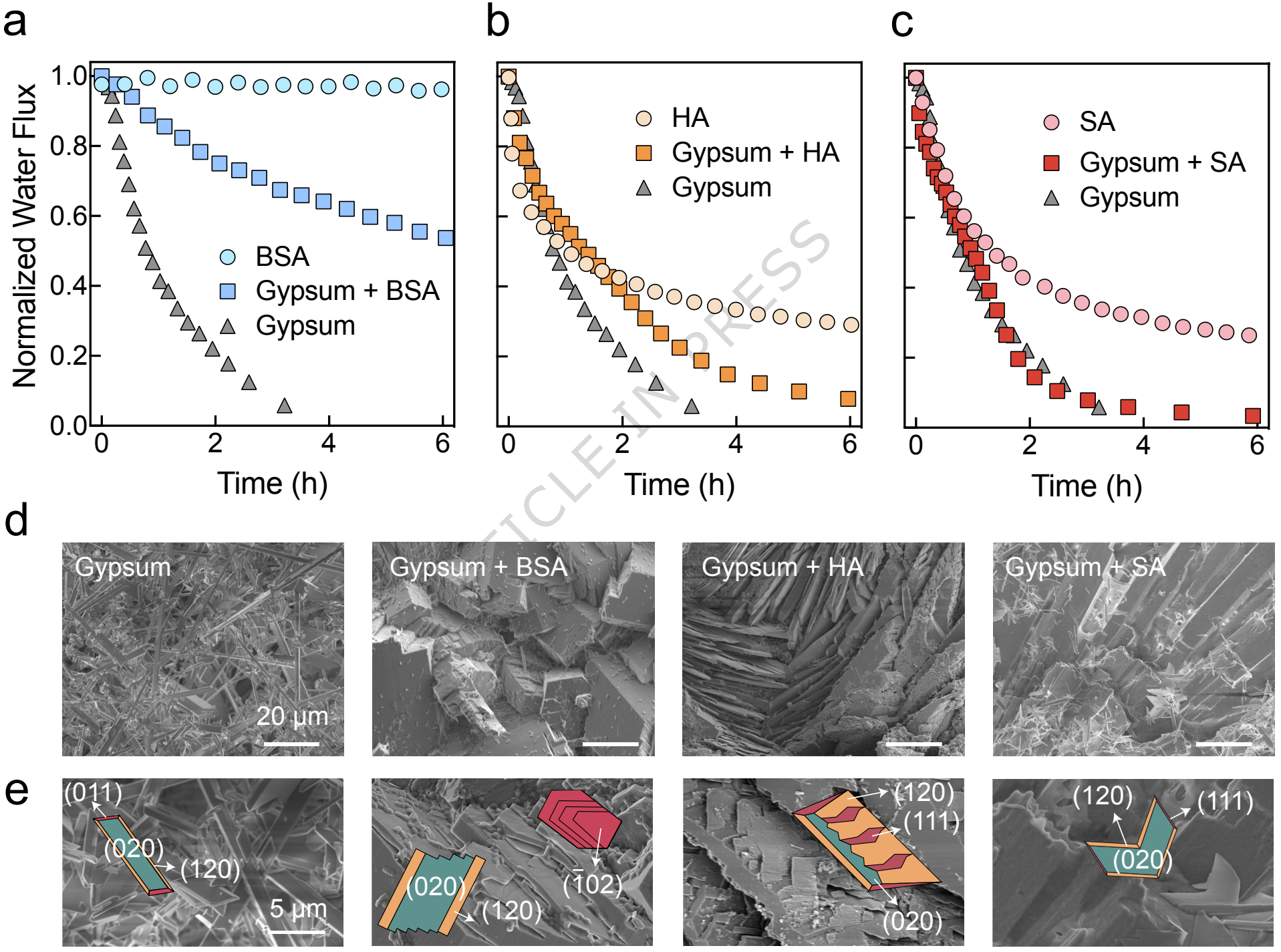
a
b
c
Normalized Water Flux
1.0
0.8
0.6
0.4
0.2
0.0
0
2
4
6
Time (h)
BSA
Gypsum + BSA
Gypsum
HA
Gypsum + HA
Gypsum
SA
Gypsum + SA
Gypsum
d
Gypsum
20 μm
Gypsum + BSA
Gypsum + HA
Gypsum + SA
e
(011)
(020)
(120)
5 μm
(020)
(120)
(102)
(120)
(111)
(020)
(120)
(111)
(020)

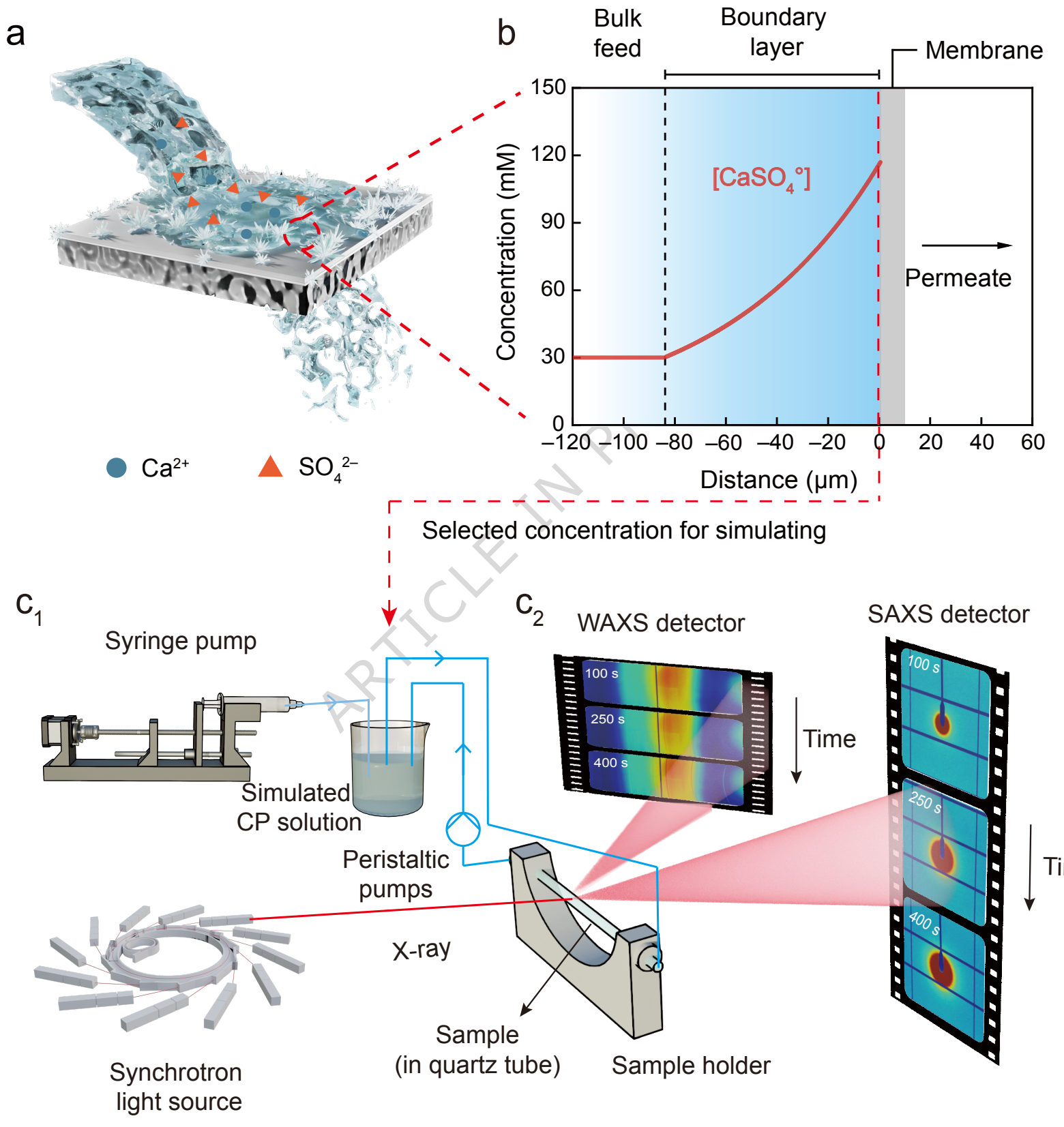

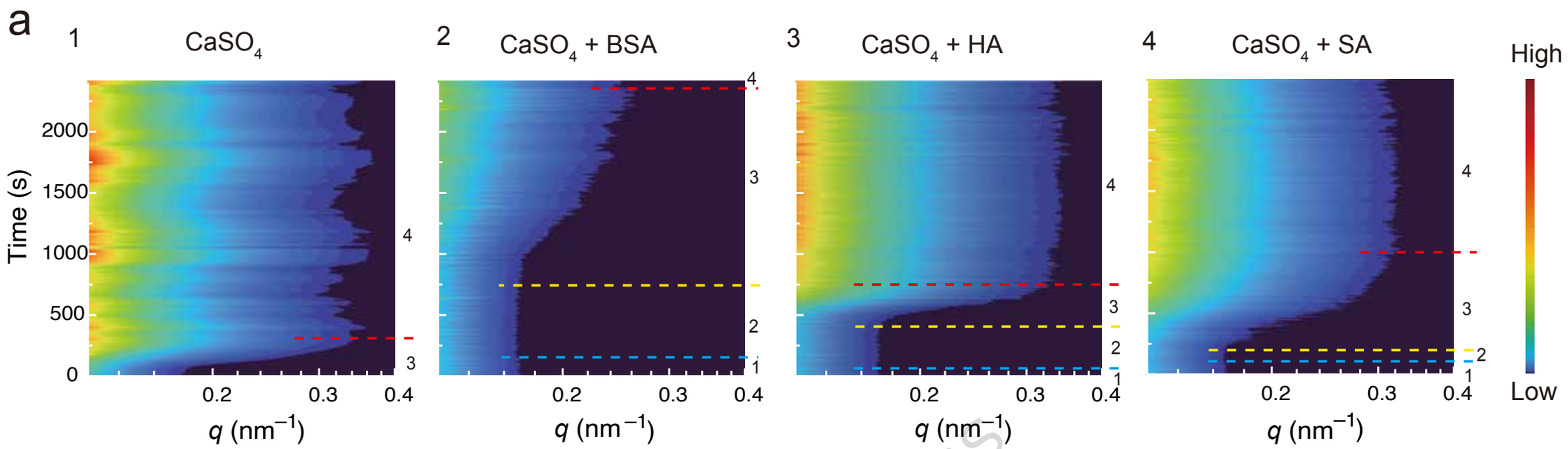
a
1
CaSO4
2
CaSO4 + BSA
3
CaSO4 + HA
4
CaSO4 + SA
High
Low
Time (s)
0
500
1000
1500
2000
0.2
0.3
0.4
q (nm−1)
1
2
3
4

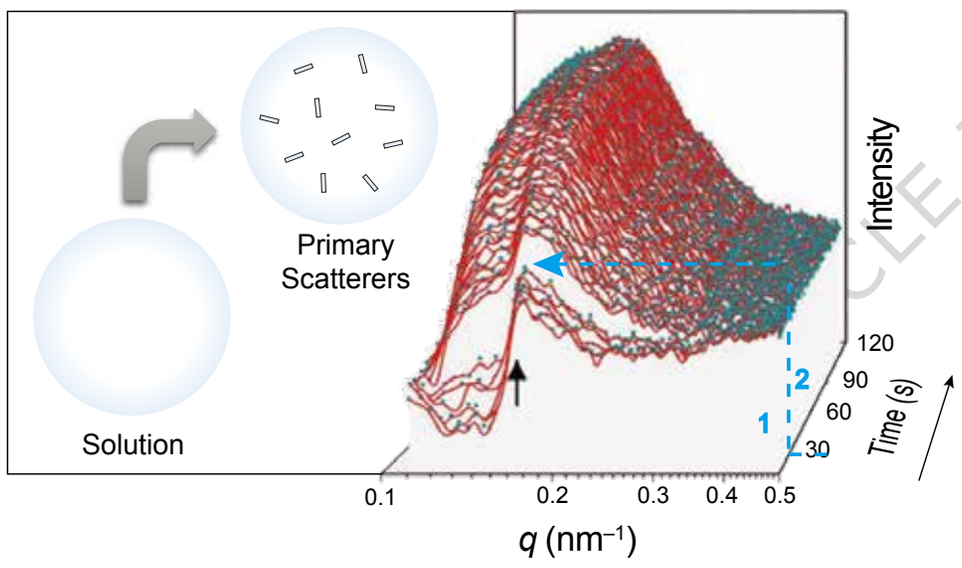
b
Primary
Scatterers
Solution
Intensity
Time (s)
30
60
90
120
0.1
0.2
0.3
0.4
0.5
q (nm−1)
1
2

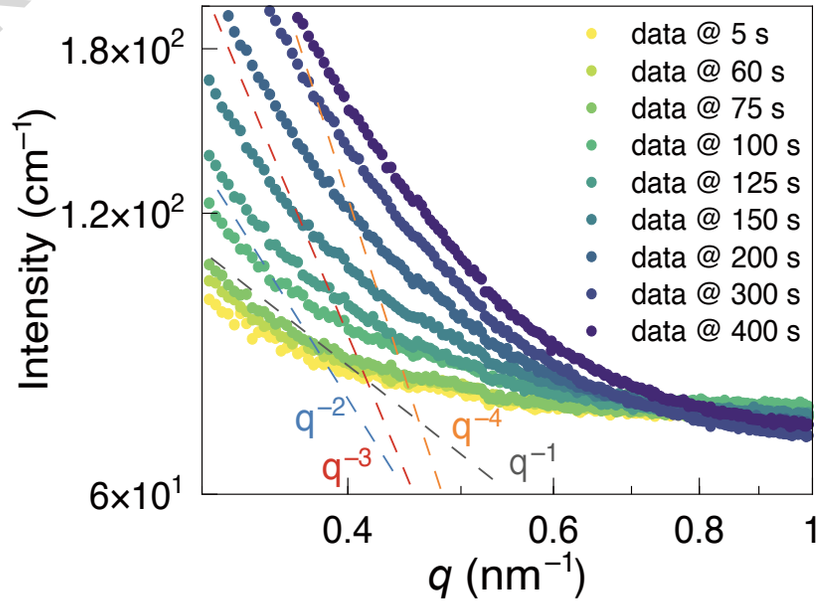
d
Intensity (cm−1)
1.8×10²
1.2×10²
6×10¹
0.4
0.6
0.8
1
q (nm−1)
data @ 5 s
data @ 60 s
data @ 75 s
data @ 100 s
data @ 125 s
data @ 150 s
data @ 200 s
data @ 300 s
data @ 400 s
q−2
q−4
q−3
q−1

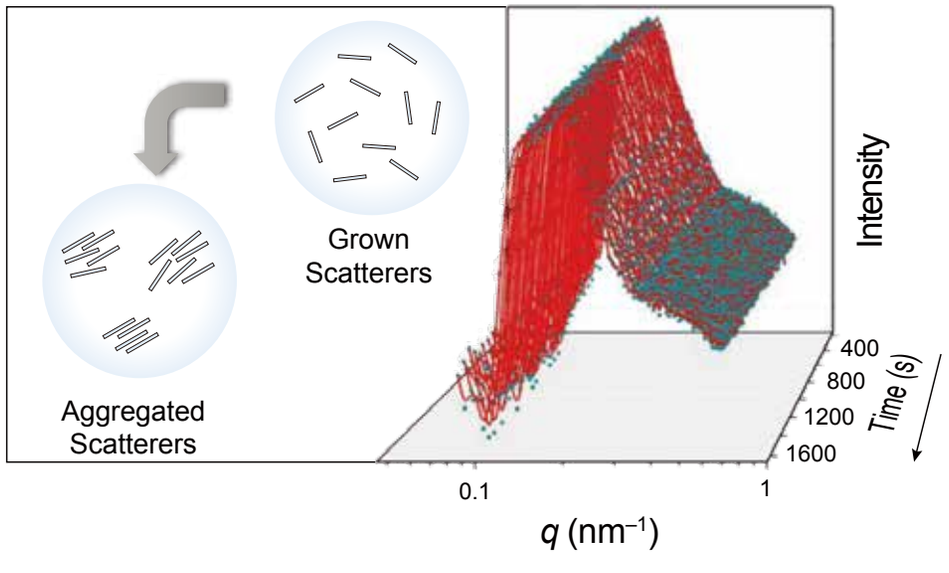
c
Grown
Scatterers
Aggregated
Scatterers
Intensity
Time (s)
400
800
1200
1600
0.1
1
q (nm−1)

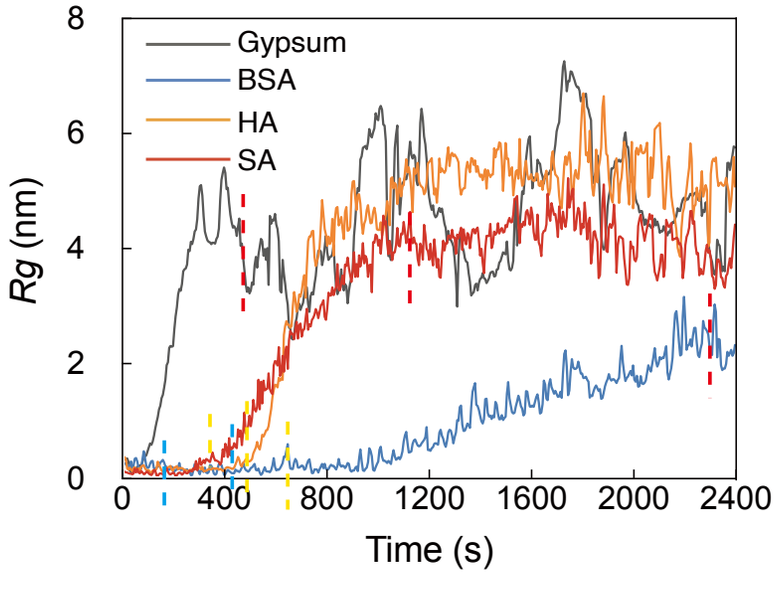
e
Rg (nm)
0
2
4
6
8
0
400
800
1200
1600
2000
2400
Time (s)
Gypsum
BSA
HA
SA

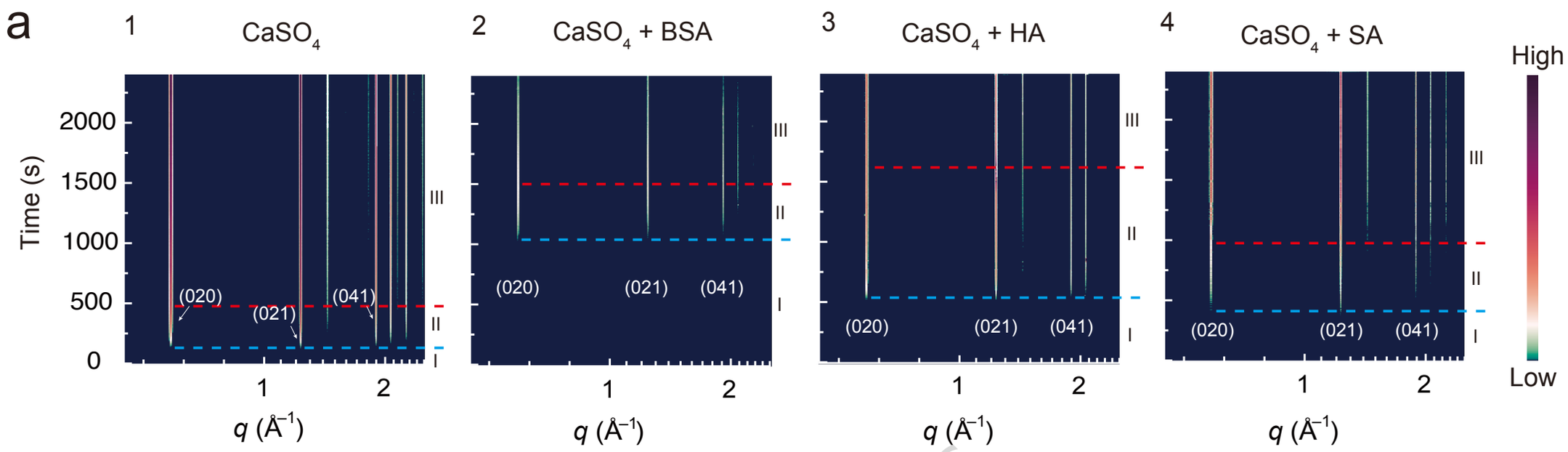
a
1
CaSO4
2
CaSO4 + BSA
3
CaSO4 + HA
4
CaSO4 + SA
Time (s)
2000
1500
1000
500
0
(020)
(021)
(041)
III
II
I
1
2
q (Å−1)
High
Low

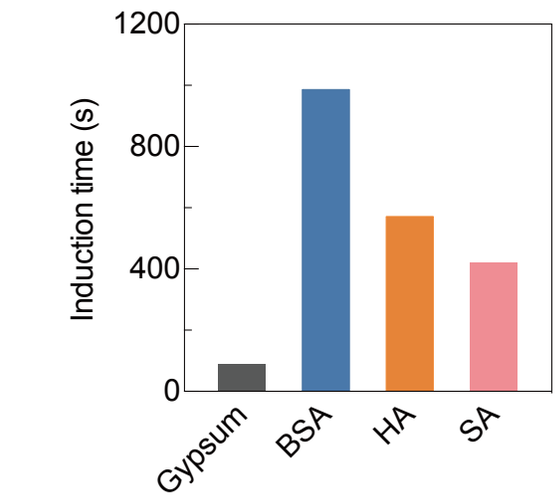
b
Induction time (s)
1200
800
400
0
Gypsum
BSA
HA
SA

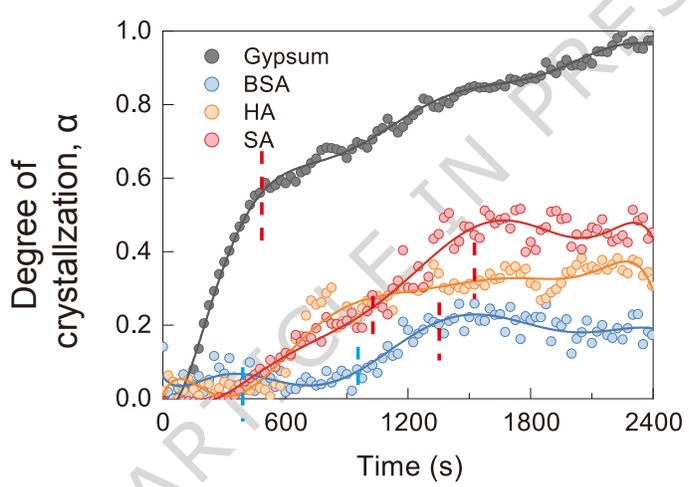
c
Degree of crystallization, α
1.0
0.8
0.6
0.4
0.2
0.0
Gypsum
BSA
HA
SA
0
600
1200
1800
2400
Time (s)

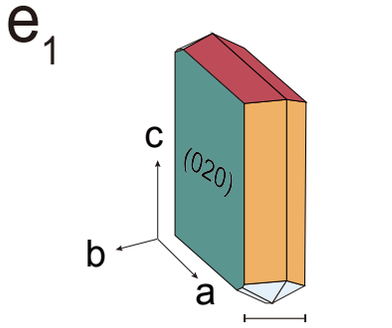
e1
c
(020)
b
a
Crystallite size

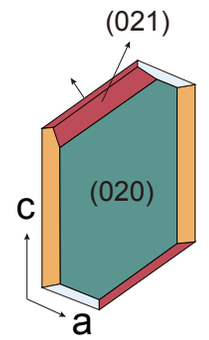
e2
(021)
(020)
c
a

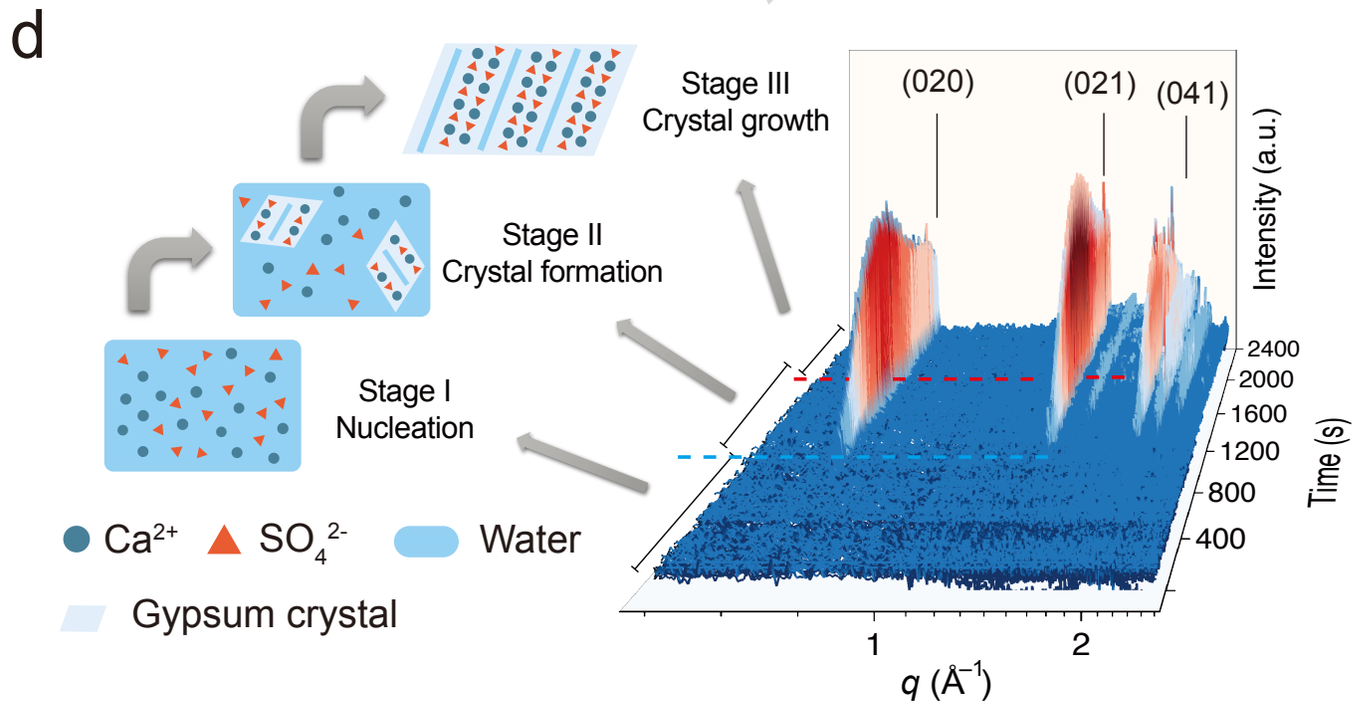
d
Stage III
Crystal growth
Stage II
Crystal formation
Stage I
Nucleation
Ca2+
SO4 2-
Water
Gypsum crystal
(020)
(021)
(041)
Intensity (a.u.)
Time (s)
2400
2000
1600
1200
800
400
1
2
q (Å−1)

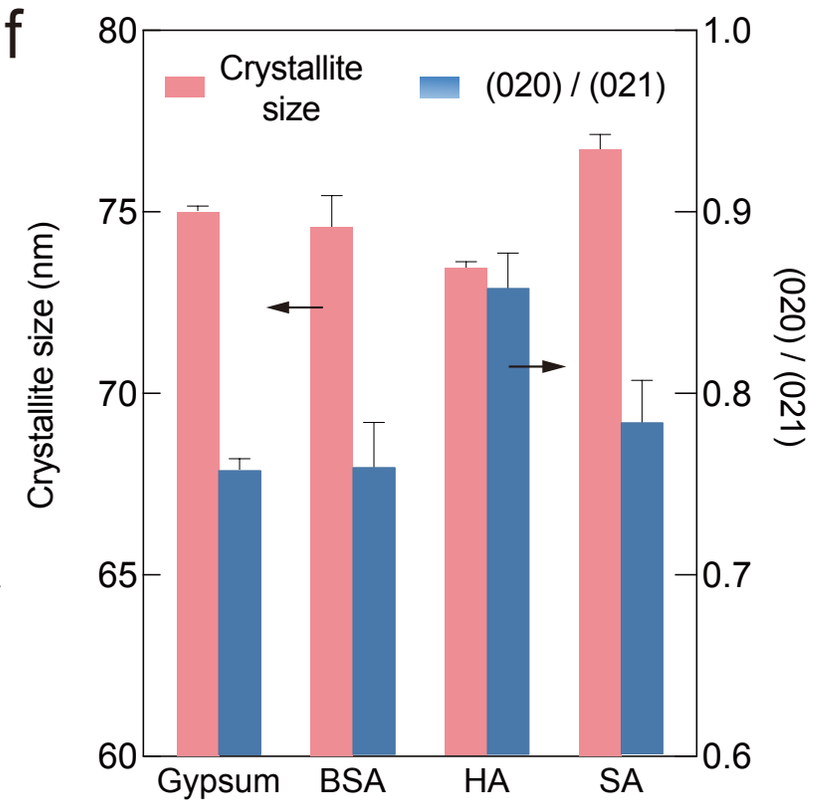
f
Crystallite size
(020) / (021)
Crystallite size (nm)
80
75
70
65
60
1.0
0.9
0.8
0.7
0.6
Gypsum
BSA
HA
SA

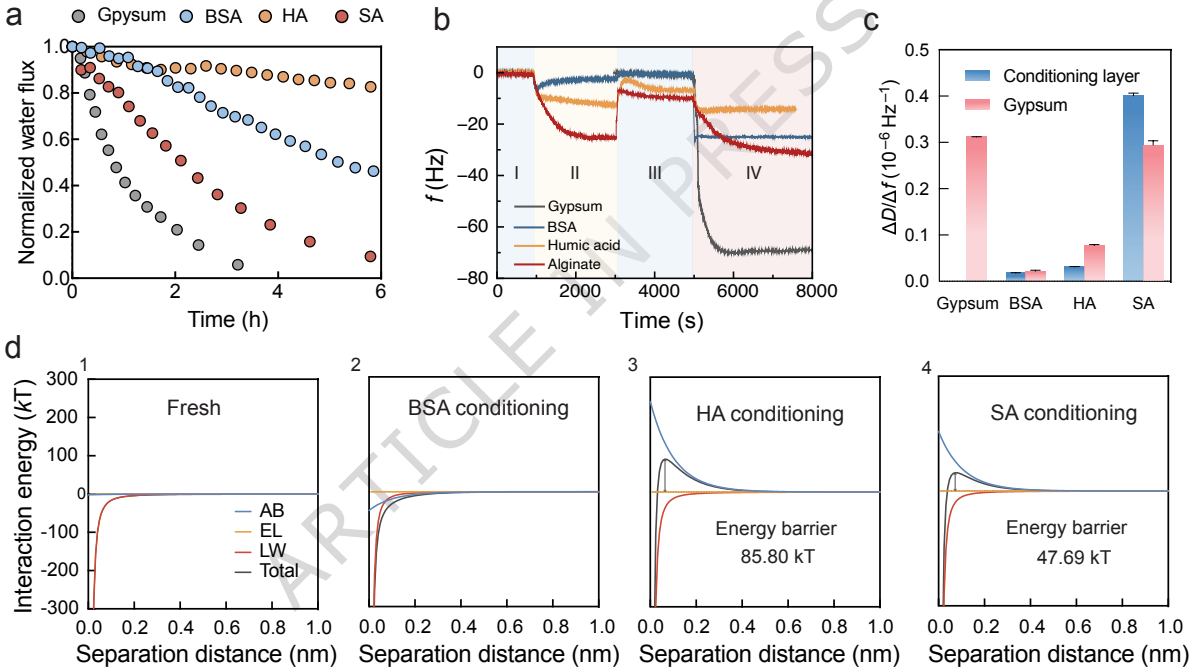

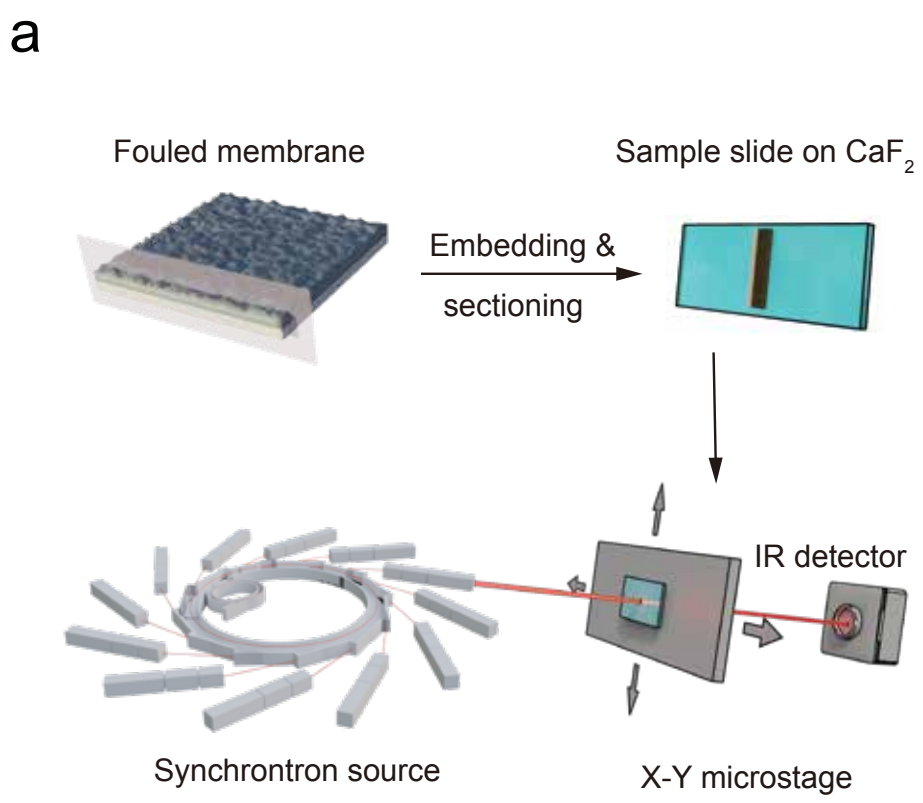
a
Fouled membrane
Sample slide on CaF_2
Embedding &
sectioning
IR detector
Synchrontron source
X-Y microstage

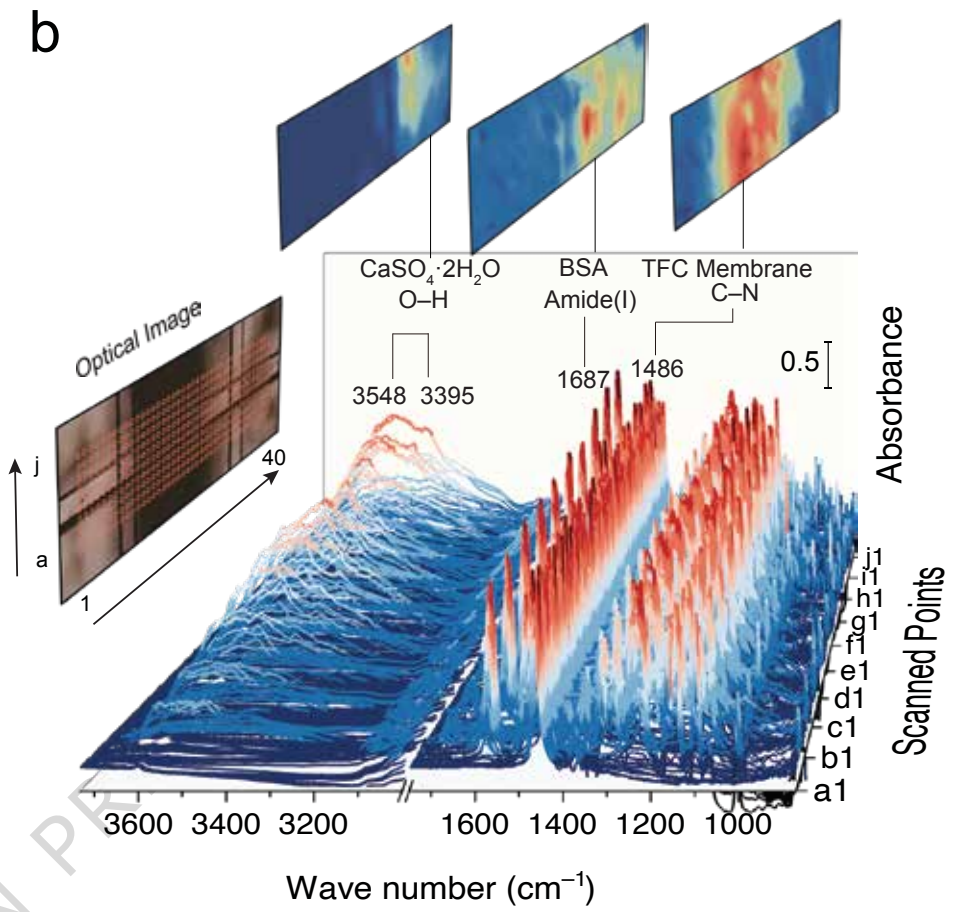
b
Optical Image
j
a
1
40
$CaSO_4 \cdot 2H_2O$
O–H
BSA
Amide(I)
TFC Membrane
C–N
3548 3395
1687
1486
0.5
Absorbance
Scanned Points
j1
i1
h1
g1
f1
e1
d1
c1
b1
a1
3600 3400 3200
1600 1400 1200 1000
Wave number (cm^{-1})

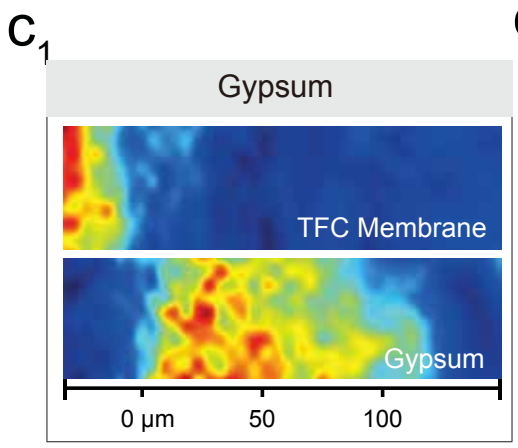
c_1
Gypsum
TFC Membrane
Gypsum
0 μm 50 100

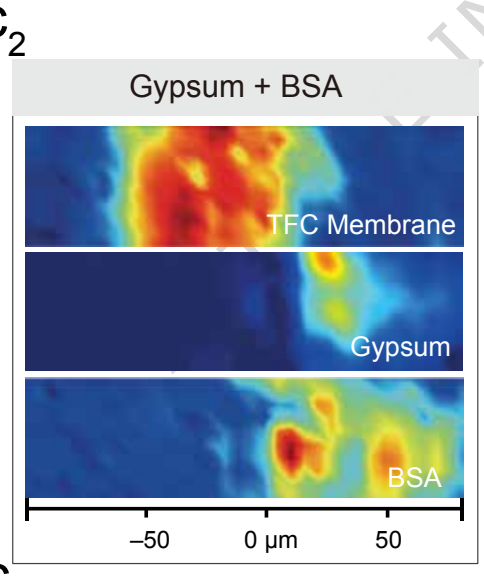
c_2
Gypsum + BSA
TFC Membrane
Gypsum
BSA
–50 0 μm 50

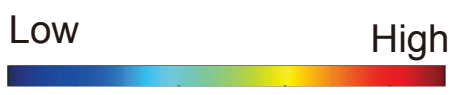
Low
High

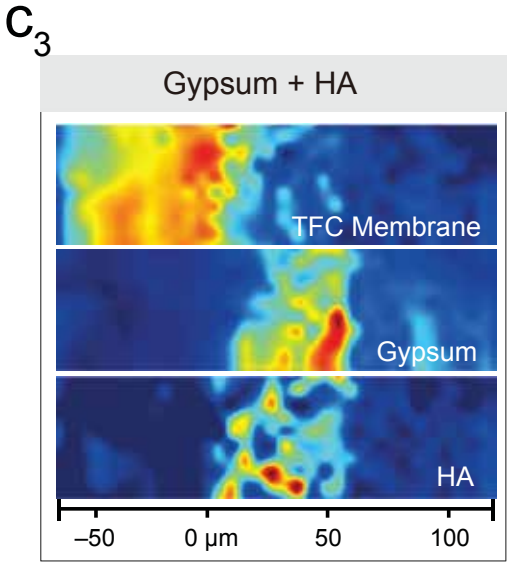
c_3
Gypsum + HA
TFC Membrane
Gypsum
HA
–50 0 μm 50 100

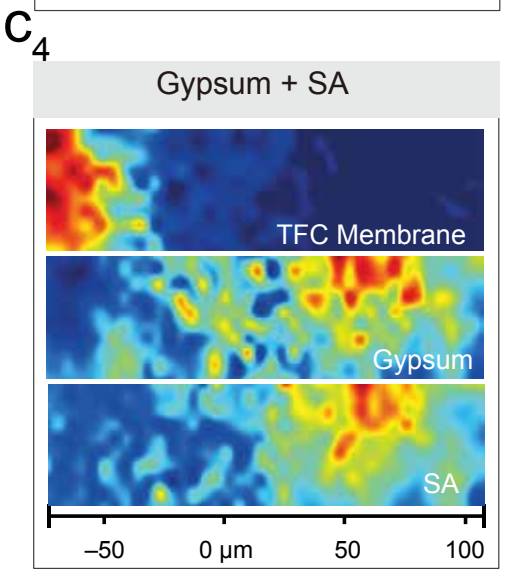
c_4
Gypsum + SA
TFC Membrane
Gypsum
SA
–50 0 μm 50 100

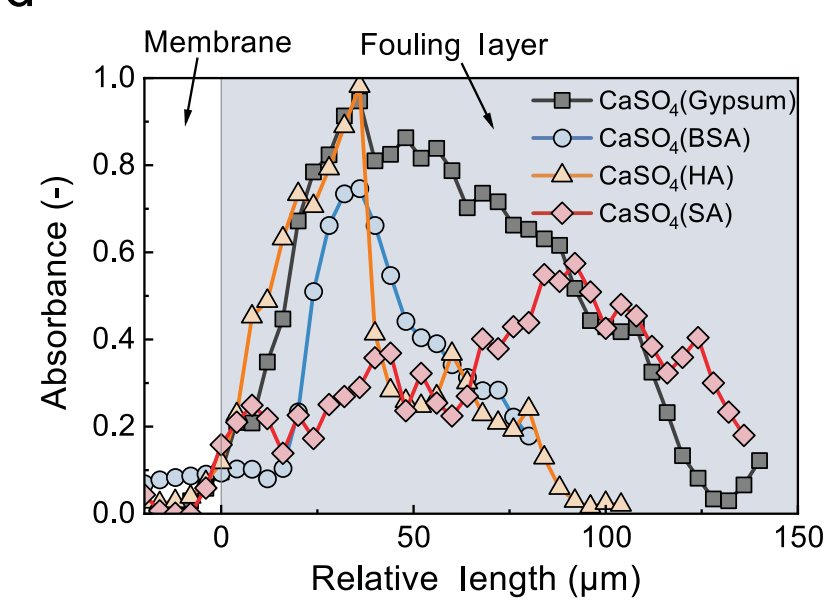
d
Membrane
Fouling layer
$CaSO_4$(Gypsum)
$CaSO_4$(BSA)
$CaSO_4$(HA)
$CaSO_4$(SA)
Absorbance (-)
1.0
0.8
0.6
0.4
0.2
0.0
0 50 100 150
Relative length (μm)

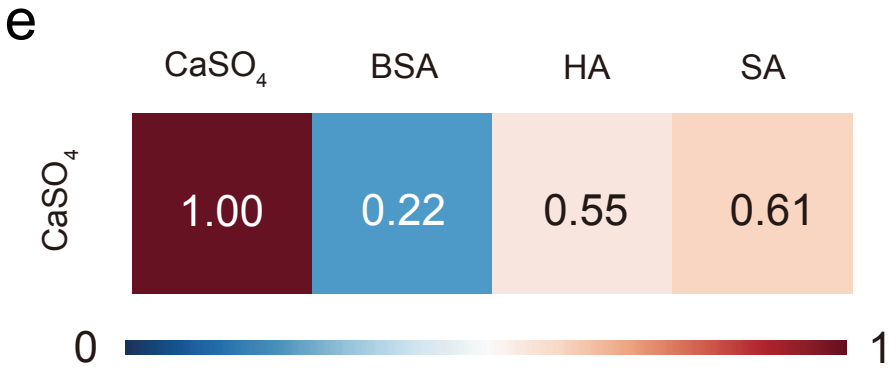
e
$CaSO_4$
BSA
HA
SA
$CaSO_4$
1.00
0.22
0.55
0.61
0
1